TURUN YLIOPISTO
UNIVERSITY OF TURKU

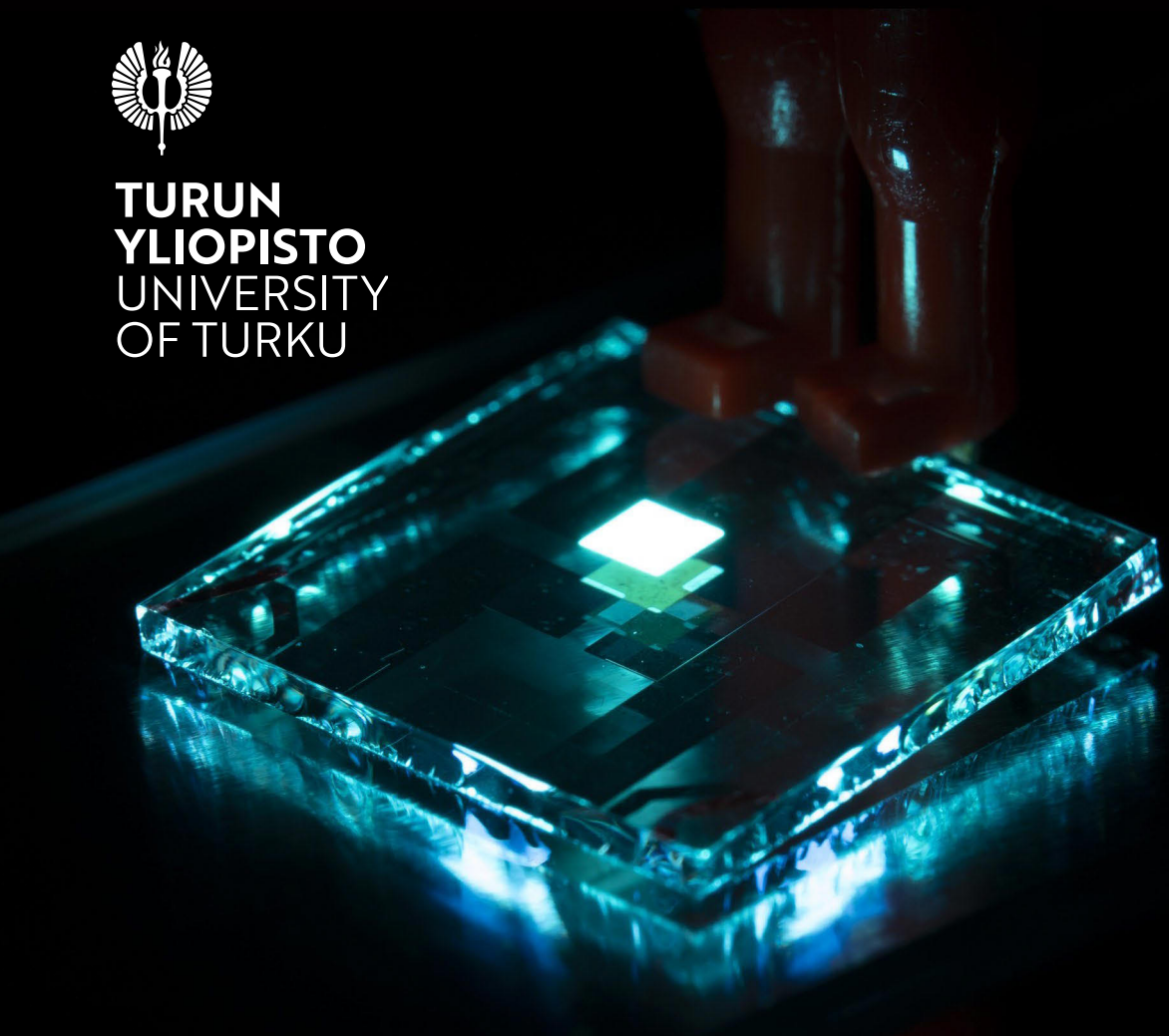

Strong Light-Matter Interaction for Efficient Organic Optoelectronics

Ahmed Gaber Abdelmagid

TURUN YLIOPISTON JULKAISUJA – ANNALES UNIVERSITATIS TURKUENSIS
SARJA – SER. F OSA – TOM. 66 | TECHNICA – INFORMATICA | TURKU 2025

TURUN
YLIOPISTO
UNIVERSITY
OF TURKU

STRONG LIGHT-MATTER INTERACTION FOR EFFICIENT ORGANIC OPTOELECTRONICS

Ahmed Gaber Abdelmagid

TURUN YLIOPISTON JULKAISUJA ANNALES UNIVERSITATIS TURKUENSIS
SARJA SER. F OSA TOM. 66 | TECHNICA INFORMATICA | TURKU 2025

University of Turku

Faculty of Technology
Department of Mechanical and Materials Engineering
Materials Engineering
Doctoral programme of Technology

Supervised by

Assoc. Prof., Konstantinos Daskalakis
University of Turku
Turku, Finland

PhD, Emilia Palo
University of Turku
Turku, Finland

Reviewed by

Professor, Jussi Toppari
University of Jyväskylä
Jyväskylä, Finland

Assoc. Prof., Giuliana Di Martino
Univeristy of Cambridge
Cambridge, United Kingdom

Opponent

Professor, Karl Börjesson
University of Gothenburg
Gothenburg, Sweden

ISBN 978-952-02-0397-9 (PRINT)
ISBN 978-952-02-0398-6 (PDF)
ISSN 2736-9390 (Painettu/Print)
ISSN 2736-9684 (Sähköinen/Online)
Painosalama, Turku, Finland 2025

إِلَى مَنْ سَخَّرَ لَنَا هَذَا الْكَوْنَ بِقَوَانِينِهِ الْمُحْكَمَةِ، وَجَعَلَ فِي تَأَمُّلِهِ عِبَادَةً،
أُهْدِي هَذَا الْجُهْدَ فِي عِلْمٍ هُوَ مِنْ آثَارِ قُدْرَتِهِ،
سَائِلًا أَنْ يَكُونَ خُطْوَةً فِي طَرِيقِ الْعِلْمِ، وَطَاعَةً فِي دَرْبِ الْيَقِينِ

To Allah—the One who has subjected this universe to us with its precise laws, and made contemplation of it an act of worship,
I dedicate this effort in a science that is among the traces of His power, asking that it be a step on the path of knowledge and an act of obedience on the road to certainty.

UNIVERSITY OF TURKU
Faculty of Technology
Department of Mechanical and Materials Engineering
Materials Engineering
ABDELMAGID, AHMED GABER: Strong Light-Matter Interaction For Efficient Organic Optoelectronics
Doctoral dissertation, 123 pp.
Doctoral programme of Technology
September 2025

ABSTRACT

Polaritons, hybrid light–matter quasiparticles formed under strong coupling, have emerged as a promising platform to reshape molecular energy landscapes and enable room-temperature control of photophysical processes. Yet despite substantial progress, polariton-based devices still trail state-of-the-art optoelectronics. This gap in polaritronics motivates this dissertation to translate polaritonic design principles into high-performance organic optoelectronic devices.

First, time-resolved electroluminescence in polaritonic organic light-emitting diodes is used to identify the origin of delayed emission under electrical drive. Despite large Rabi splittings and systematic tuning of the lower polariton relative to the triplet manifold, the delayed component is dominated by trap-assisted emission, with no resolvable polariton-enabled triplet harvesting under the measured conditions. This highlights the collective, delocalized nature of polaritons as a key limitation for modifying intramolecular kinetics in these devices.

Building on these insights, the thesis pivots to device-scale polaritonic engineering. For organic photodiodes, non-fullerene acceptors are embedded in a microcavity to form polaritons, delivering narrowband, angle-stable responsivity by operating the lower polariton on the low-absorption tail, where its excitonic fraction suppresses angular dispersion while maintaining useful responsivity. The result is a tunable, intrinsically selective passband with markedly reduced angular shift compared with conventional cavity organic photodiodes.

For near-infrared organic light-emitting diodes, a broadband deep-red emitter is combined with a strong-coupling layer in a first-order microcavity. The resulting devices exhibit lower polariton-dominated electroluminescence with competitive efficiencies. Furthermore, emission bandwidths are substantially narrower than typical near-infrared organic devices, concentrating emission in the near-infrared.

Also, strong coupling and lower-polariton emission have been realised in hybrid and fully solution-processed DBR microcavities.

Overall, the work clarifies when polaritons do *not* alter microscopic relaxation pathways in organic light-emitting diodes, and shows how polaritonic engineering nevertheless delivers practical gains, namely, narrowband, angle-independent organic photodiodes and record-class near-infrared organic light-emitting diodes efficiencies, thereby bridging fundamental polariton science and device performance.

KEYWORDS: organic polaritons; near-infrared OLEDs; organic photodiodes.

TURUN YLIOPISTO
Teknillinen tiedekunta
Kone- ja materiaalitekniikan laitos
Materiaalitekniikka
ABDELMAGID, AHMED GABER: Strong Light-Matter Interaction For Efficient Organic Optoelectronics
Väitöskirja, 123 s.
Teknologian tohtoriohjelma
Syyskuu 2025

TIIVISTELMÄ

Polaritonit - valon ja aineen vahvassa vuorovaikutuksessa hybridisoituessaan muodostamat kvasihiukkaset - ovat nousseet lupaavaksi keinoksi muokata molekyylien energiaympäristöä ja hallita fotofysikaalisia prosesseja jopa huoneenlämmössä. Merkittävästä tutkimuskehityksestä huolimatta polaritoneihin perustuvat laitteet ovat yhä jäljessä perinteisestä huipputason optoelektroniikasta. Tämä väitöskirja tarkastelee, miten polaritonien suomia etuja voidaan soveltaa suorituskykyisten orgaanisten optoelektronisten teknologioiden suunnittelussa. Ensimmäisessä osassa polaritonisten OLED-laitteiden viivästyneen emission alkuperä selvitetään analysoimalla niiden aikariippuvaa elektroluminesenssia. Tulokset osoittavat, että viivästyneessä elektroluminesenssissa ansa-avusteinen emissio dominoi eikä polaritonien mahdollistamaa triplettien hyödyntämistä havaita. Tämä korostaa sitä, miten polaritonien kollektiivinen delokalisoitunut luonne rajoittaa merkittävästi niiden hyödyntämistä molekyylin sisäisen kinetiikan muokkaamiseen. Näitä löydöksiä hyödyntäen työ keskittyy seuraavaksi laitetason polaritoniseen suunnitteluun. Orgaaninen fotodiodi muodostetaan upottamalla fullereenittomia akseptorimolekyyleja mikrokaviteettiin, minkä ansiosta muodostuvaa alempaa polaritonia hyödyntämällä diodin responsiivisuudesta saadaan kapeakaistainen ja kulmavakaa. Tuloksena on säädettävä ja selektiivinen kaista, jonka kulmasiirtymä on huomattavasti pienempi kuin perinteisissä orgaanisissa kaviteetti-fotodiodeissa. Lähi-infrapunan OLED-laitteet puolestaan valmistetaan yhdistämällä laajakaistainen syvänpunainen emittoija ensimmäisen kertaluvun mikrokaviteetin vahvasti kytkettyyn kerrokseen. Tämän avulla saavutetaan alemman polaritonin hallitsema elektroluminesenssi ja kilpailukykyinen hyötysuhde. Lisäksi se johtaa hyvin lähi-infrapunaan rajoittuviin emissiokaistoihin, jotka ovat merkittävästi kapeampia kuin tyypillisissä lähi-infrapunan orgaanisissa laitteissa. Yhteenvetona väitöskirja selventää, milloin polaritonit eivät vaikuta mikroskooppisiin relaksaatiopolkuihin OLED-laitteissa ja osoittaa, miten polaritonehin perustuva suunnittelu voi siitä huolimatta tuottaa konkreettisia etuja: kapeakaistaiset ja kulmasta riippumattomat fotodiodit sekä ennätystason lähi-infrapunan OLED-hyötysuhteet. Tällä tavoin tutkimus yhdistää perustavanluonteisen polaritonitieteen ymmärryksen orgaanisen optoelektroniikan suorituskyvyn parantamiseen.

ASIASANAT: orgaaniset polaritonit, mikrokaviteetit, lähi-infrapunan OLEDit, orgaaniset fotodiodit.

Acknowledgements

First and foremost, *Alhamdulillah*—praise and thanks be to Allah—for granting me the strength, patience, and clarity to complete this thesis.

I am deeply grateful to my supervisor, Dr. Konstantinos S. Daskalakis, for his guidance, trust, and steady support. Your insights and encouragement shaped my thinking and helped me grow as an independent researcher. I would like to extend my gratitude to my second supervisor, Dr. Emilia Palo, for her support during my onboarding and my first steps at the University of Turku.

To my colleagues in the LMD group: thank you for the whiteboard ideas, constructive debates, and day-to-day camaraderie that made hard days lighter—I learned from each of you. Thank you, Manish, Mike, Olli, Henri, and Oskar, for your support, help, and good company; and thanks as well to Rustem, Gabriel, and Akseli for their assistance whenever needed. A special thanks to my colleague and fellow PhD researcher, Hassan A. Qureshi, with whom I worked side by side—designing experiments, debating ideas, and often discussing almost everything. Your rigor, patience, and good humor made the tough days manageable and the good days even better. Wishing you all the best in the final stretch of your PhD.

To my collaborators across institutions and time zones, thank you for your generosity with data, facilities, and expertise. In particular, I am grateful to Prof. Thomas Anthopoulos, Dr. Nicola Gasparini, Dr. Seyhan Salman, and Dr. Kimmo Luoma. Joint work and discussions enriched this work far beyond what I could have achieved alone.

To the host of my research internship, the Gather Lab at the University of Cologne: thank you for the warm welcome, access to facilities, and the collegial atmosphere that accelerated key parts of this thesis. I am especially thankful to Prof. Malte Gather and Dr. Andreas Mischok for their mentorship and support during my stay.

I am sincerely grateful to the pre-examiners, Prof. Jussi Toppari and Dr. Giuliana Di Martino, for their careful reading and constructive feedback.

To my friends, near and far, who checked in, listened, and celebrated the small wins. Warm thanks to my Finland-based friends—Ali, Beltagy, Ibrahim, Mahmoud, Omar, Osama, M. Waleed, A. Soliman, and Dr. Mohamed—for shared meals, steady support, and good humor through long days and late nights. A special thanks to my friend Ali—whose long stay by my side and all-around support, from day-to-day help to practical advice, made this journey lighter. A special thanks as well to my friend Mustafa—far in distance yet close in every way—whose steady support, thoughtful listening, and honest counsel meant a great deal.

إِلَى عَائِلَتِي الكَرِيمَةِ: إِلَى أُمِّي، دُعَاؤُكِ وَسَنَدُكِ الدَّائِمَانِ كَانَا عُدَّتِي فِي الطَّرِيقِ، وَمَحَبَّتُكِ الثَّابِتَةُ هِيَ مَا يَشُدُّ أَزْرِي كُلَّمَا ثَقُلَ الحِمْلُ. وَإِلَى أَخِي الَّذِي لَمْ يَتَرَاجَعْ دَعْمُهُ وَإِيمَانُهُ بِي يَوْمًا، جَزَاكُمَا اللهُ عَنِّي خَيْرًا، وَشُكْرًا لِوُقُوفِكُمَا بِجَانِبِي فِي كُلِّ خُطْوَةٍ. إِلَى آدم وعبدالرحمن: فضولكما وطاقتكما وأسئلتكما أبقتني مُبتسمًا وذكَّرتني بأنَّ التعلّم متعةٌ دائمة، وكانت مكالماتكما دعمًا ينهض بي حين يطولُ النهار

إِلَى إيناس، زَوْجَتِي الحَبِيبَةِ، رَفِيقَةِ الدَّرْبِ وَالعِلْمِ؛ كُنْتِ أُنْسَ الرُّوحِ فِي البَيْتِ، وَرَفِيقَةَ الفِكْرِ فِي المَعْمَلِ. بِصَبْرِكِ وَحَنَانِكِ وَثِقَتِكِ بِي مَضَتْ هَذِهِ الرِّسَالَةُ خُطْوَةً بَعْدَ أُخْرَى. وَفِي البَحْثِ كُنْتِ عَوْنًا بِعَيْنِ البَاحِثَةِ وَخِبْرَتِهَا؛ بِأَسْئِلَتِكِ الهَادِئَةِ، وَمُلَاحَظَاتِكِ العَمَلِيَّةِ، وَحِوَارَاتِنَا الَّتِي امْتَدَّتْ حَتَّى آخِرِ اللَّيْلِ. لَكِ مِنِّي شُكْرٌ لَا يَخْفُتُ، وَمَحَبَّةٌ لَا تَنْقُصُ؛ فَهَذِهِ الرِّسَالَةُ ثَمَرَةُ قَلْبَيْنِ، أُهْدِيكِ إِيَّاهَا.

To my wife—my partner, friend, and constant source of patience and joy. Your encouragement and faith in me made this work possible, and your thoughtful scientific support throughout the research—from critical questions to practical advice and late-night brainstorming—kept the project on track. This thesis is as much yours as it is mine.

Finally, I gratefully acknowledge the European Research Council (ERC) under the European Union's Horizon 2020 research and innovation programme (grant agreement No. 948260) for supporting my PhD. I also thank Suomalainen Tiedeakatemia, Svenska tekniska vetenskapsakademien i Finland, and Turku University Foundation for funding that enabled my research stay in Germany.

Turku, the 29^{th} of September 2025
Ahmed Gaber Abdelmagid

Table of Contents

Abbreviations

LCAO	Linear combination of atomic orbitals
HOMO	Highest occupied molecular orbital
LUMO	Lowest unoccupied molecular orbital
S_0	Ground state
S_1	Excited singlet state
T_1	Triplet state
PES	Potential energy surface
LE	Locally excited state
CT	Charge transfer state
OPD	Organic photodiode
OLED	Organic light-emitting diode
EQE	External quantum efficiency
IQE	Internal quantum efficiency
IC	Internal conversion
FWHM	Full width at half maximum
ISC	Intersystem crossing
RISC	Reverse intersystem crossing
ΔE_{ST}	Singlet–triplet energy gap
NIR	Near-infrared
PLQY	Photoluminescence quantum yield
D	Donor
A	Acceptor
FRET	Förster energy transfer
DET	Dexter energy transfer
LP	Lower polariton
MP	Middle polariton
UP	Upper polariton
ITO	Indium tin oxide
HTL	Hole transport layer
EML	Emissive layer
ETL	Electron transport layer
FE	Fluorescent emitter
PE	Phosphorescent emitter

TADF	Thermally activated delayed fluorescence
TCSPC	Time-correlated single-photon counting
EL	Electroluminescence
AREL	Angle-resolved electroluminescence
TTA	Triplet–triplet annihilation
TE	Trap emission
MoO_3	Molybdenum trioxide
LiF	Lithium fluoride
SCL	Strong coupling layer
C_{60}	Fullerene
TAPC	1,1-bis(di-4-tolylaminophenyl)cyclohexane
TCTA	Tris(4-carbazoyl-9-ylphenyl)amine
mCP	1,3-bis(N-carbazolyl)benzene
DCN-SPTPA	3-(4-(9,9'–Spirobi[fluoren]-2-yl(phenyl)amino)phenyl)dibenzo[a,c]phenazine-11,12-dicarbonitrile
CBP	4,4'–bis(N-carbazolyl)-1,1'–biphenyl
TmPyPB	1,3,5-tri(m-pyrid-3-yl-phenyl)benzene

List of Original Publications

This dissertation is based on the following original publications, which are referred to in the text by their Roman numerals:

I **Ahmed Gaber Abdelmagid**, Hassan A. Qureshi, Michael A. Papachatzakis, Olli Siltanen, Manish Kumar, Ajith Ashokan, Seyhan Salman, Kimmo Luoma, and Konstantinos S. Daskalakis. "Identifying the origin of delayed electroluminescence in a polariton organic light-emitting diode". *Nanophotonics*, 2024; 14: 2565-2573.

II **Ahmed Gaber Abdelmagid**, Zhuoran Qiao, Boudewijn Coenegracht, Gaon Yu, Hassan A. Qureshi, Thomas D. Anthopoulos, Nicola Gasparini, and Konstantinos S. Daskalakis. "Polaritons in non-fullerene acceptors for high responsivity angle-independent organic narrowband infrared photodiodes". *Advanced Optical Materials*, 2025; e01727.

III **Ahmed Gaber Abdelmagid**, Andreas Mischok, Malte C. Gahter, Konstantinos S. Daskalakis. "Polaritonic Engineering for High-Performance Near-Infrared OLEDs". *Manuscript under preparation*, 2025.

IV Emilia Palo, Michael A. Papachatzakis, **Ahmed Gaber Abdelmagid**, Hassan A. Qureshi, Manish Kumar, Mikko Salomäki, and Konstantinos S. Daskalakis. "Developing solution-processed distributed Bragg reflectors for microcavity polariton applications". *The Journal of Physical Chemistry C*, 2023; 127(29):14255–14262.

V Hassan A. Qureshi, Michael A. Papachatzakis, **Ahmed Gaber Abdelmagid**, Mikko Salomäki, Ermei Mäkilä, Oskar Tuomi, Olli Siltanen, and Konstantinos S. Daskalakis. "Giant Rabi Splitting and Polariton Photoluminescence in an all Solution-Deposited Dielectric Microcavity". *Advanced Optical Materials*, 2025; 13(16):2500155.

Publications produced but not included in this doctoral thesis:

- Kumar M, Dutta A, Qureshi HA, Papachatzakis MA, **Abdelmagid AG**, Daskalakis KS. Single-Emitter White OLEDs via Microcavity Spectral Engineering. *Advanced Optical Materials*. 2025:e01358.
- Leppälä T, **Abdelmagid AG**, Qureshi HA, Daskalakis KS, Luoma K. Linear optical properties of organic microcavity polaritons with non-Markovian quantum state diffusion. *Nanophotonics*. 2024;13(14):2479-90.

Declaration of AI use

In preparing this dissertation, generative AI tools (ChatGPT and Grammarly) were used solely for grammar, spelling, readability, and LaTeX formatting. No AI was used to develop research ideas, analyse data, or draw conclusions.

1 Introduction

Note: Several of the concepts and descriptions discussed in this chapter are adapted from the books *Electronic Processes in Organic Semiconductors* [1] for section 1.1, *Microcavities* [2] for section 1.2, and *Organic electronics: foundations to applications* [3] for section 1.3 .

1.1 Organic semiconductors

As their name suggests, organic semiconductors merge the beneficial properties of two worlds: the chemical/mechanical flexibility of organic materials and the functional electrical characteristics of semiconductors.

"Organic" means the material consists mainly of carbon and hydrogen, potentially including heteroatoms like sulfur, oxygen, or nitrogen.

"Semiconductors" refers to their ability to absorb and emit light and transport electrical charge. These core properties enable their use in optoelectronic applications like light-emitting diodes, photodiodes, and solar cells.

It is crucial to recognize that the semiconducting behavior of organic materials differs fundamentally from that of inorganic semiconductors. In particular, inorganic semiconductors like silicon (Si), germanium (Ge), and gallium arsenide (GaAs) possess relatively small band gaps. This enables significant intrinsic conductivity at room temperature, driven by thermal excitation of electrons from the valence band to the conduction band. Furthermore, their large dielectric constants significantly weaken the Coulombic attraction between electrons and holes. Consequently, light absorption directly generates free charge carriers (electrons and holes) under ambient conditions.

In contrast, organic semiconductors feature much larger band gaps coupled with low dielectric constants. This combination renders intrinsic conductivity negligible at room temperature. As a result, their conductivity relies entirely on extrinsic mechanisms, including charge injection from electrodes, chemical doping (intentional or unintentional), and the dissociation of photogenerated bound electron-hole pairs, known as excitons. Therefore, efficient organic optoelectronic devices require both a deep understanding of the electronic structure (which governs photophysical properties) and specialized engineering (e.g., heterojunctions, electrodes, transporting layers) to dissociate tightly bound excitons into free charges.

1.1.1 Orbitals in carbon atoms

The electronic structure of organic semiconductors originates from carbon, their fundamental building block. In ground state arrangements, a carbon atom has six electrons distributed as follows:

$$\text{Ground-state:} \quad 1s^2\, 2s^2\, 2p_x^1\, 2p_y^1\, 2p_z^0$$

Carbon possesses only two unpaired electrons, limiting it to form two covalent bonds. However, in molecular compounds, carbon consistently forms four bonds by promoting one electron from the $2s$ orbital to the vacant $2p_z$ orbital, achieving the following configuration:

$$\text{After promotion:} \quad 1s^2\, 2s^1\, 2p_x^1\, 2p_y^1\, 2p_z^1$$

This promotion is energetically favorable since the energy *cost* of promoting the electron is outweighed by the *net energy gain* from forming two additional bonds. When bonding atoms approach, electrostatic interactions make the $2s$ and $2p$ orbitals degenerate, enabling their hybridization into new orbitals (e.g., sp, sp^2, sp^3) optimized for directional bonding as shown in **Figure 1**. Crucially, unhybridized p-orbitals in sp^2/sp systems create π-conjugated networks, enabling charge delocalization essential for semiconductor function in organic electronics.

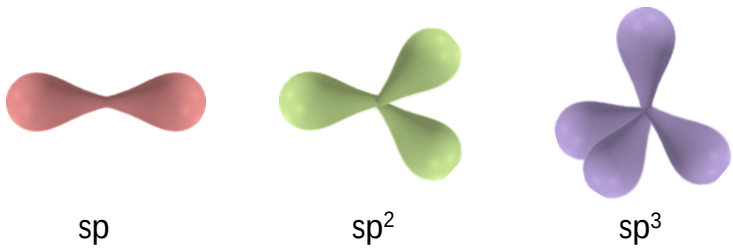

Figure 1. Hybridization and molecular geometry: (left) sp hybrids forming a linear arrangement with 180° bond angle; (middle) sp^2 hybrids giving a trigonal–planar geometry with 120° bond angles; (right) sp^3 hybrids producing a tetrahedral geometry with 109.5° bond angles.[1]

1.1.2 Molecular orbitals

The hybridization states established in the previous subsection fundamentally govern molecular bonding configurations. Chemical bonds form through pairs of shared electrons occupying molecular orbitals generated via linear combination of atomic orbitals (LCAO). Two fundamental bond types emerge from distinct orbital interactions: σ-bonds arise from *axial overlap* of hybrid orbitals, while π-bonds originate from *lateral overlap* of unhybridized p-orbitals.

In ethene (C_2H_4), this manifests through sp^2 hybridization, where each carbon atom forms three in-plane hybrid orbitals and one perpendicular $2p_z$ orbital. The sp^2 orbitals generate σ-bonds with hydrogen and the adjacent carbon, while lateral overlap of p_z orbitals creates a π-bond (**Figure 2**). The constructive in-phase overlap of adjacent carbon p-orbitals in ethene results in the formation of a low-energy π bonding orbital, while the out-of-phase overlap forms a high-energy π^* anti-bonding orbital. The π orbital is fully occupied with two electrons, making it the **highest occupied molecular orbital (HOMO)**. In contrast, the π^* orbital is unoccupied and represents the **lowest unoccupied molecular orbital (LUMO)**. This energy difference between HOMO and LUMO plays a critical role in determining the electronic and optical properties of conjugated molecules. In these systems, π-orbital delocalization across multiple atoms generates extended molecular orbitals, reducing the HOMO-LUMO gap. This bandgap engineering is paramount for organic semiconductors, which enhances charge carrier mobility, reduces photon absorption thresholds, and facilitates exciton dissociation in optoelectronic devices.

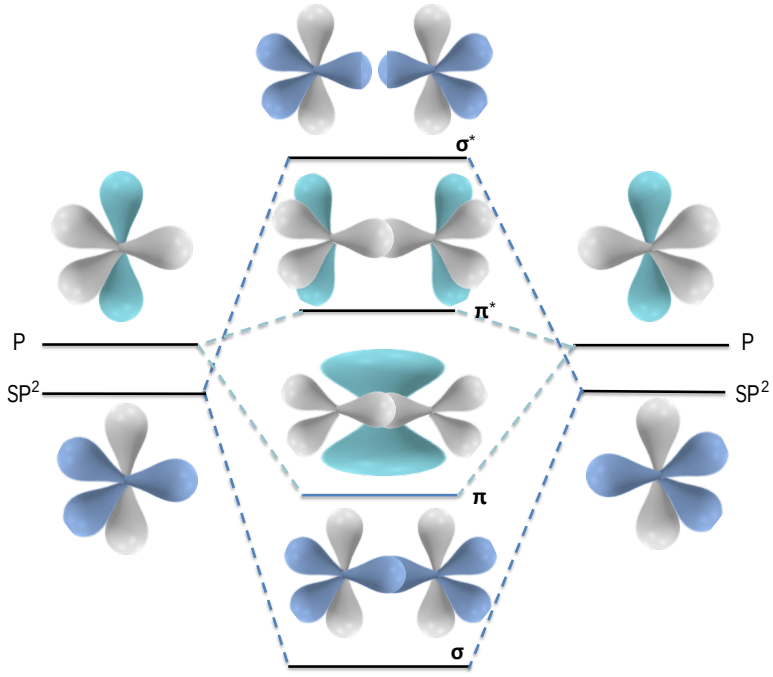

Figure 2. Qualitative molecular-orbital diagram for ethene (C_2H_4). Each carbon is sp^2-hybridized; end-on overlap of sp^2 orbitals forms the C–C σ bond (and σ^*), while lateral overlap of the unhybridized p orbitals forms the π bond (and π^*). Relative AO and MO energies and nodal character are indicated.

1.1.3 Excited states

While molecular orbital (MO) theory, via hybridization and the LCAO method, defines the potential electronic structure through one-electron energy levels, accurately describing actual excited-state phenomena necessitates distinguishing between electron configurations and many-electron states. An electron configuration describes which MOs are occupied by electrons, but does not account for electron-electron interactions. In contrast, a many-electron state fully characterizes the system through its total wavefunction, incorporating both spatial distributions and spin correlations, with an associated total energy.

Singlet and triplet states

Building on the distinction between molecular orbital configurations and many-electron states, electron spin further differentiates electronic excited states into singlet and triplet states. While the configuration such as one electron in a π (HOMO) orbital and one in a π^* (LUMO) orbital may be the same, the total spin of the electrons determines the actual quantum state of the molecule. In this context, the spin wavefunction becomes crucial, as it describes how the intrinsic angular momentum (spin) of each electron combines in the excited state. For example, two electrons in different orbitals may adopt parallel spins ($\uparrow\uparrow$, total spin $S = 1$) or antiparallel spins ($\uparrow\downarrow$, $S = 0$), generating spin-triplet or spin-singlet states, respectively.

Electron spin can be intuitively represented using a vector model, which provides a visual and dynamic depiction of spin angular momentum. In this framework, spin-up and spin-down states are represented by vectors precessing around an external axis, each tracing out a cone in opposite directions (see **Figure 3**). The quantum mechanical spin states are denoted by α and β, corresponding to the spin-up and spin-down wavefunctions of the one-electron states, respectively. These states form the basis for constructing many-electron spin wavefunctions, such as singlet and triplet combinations.

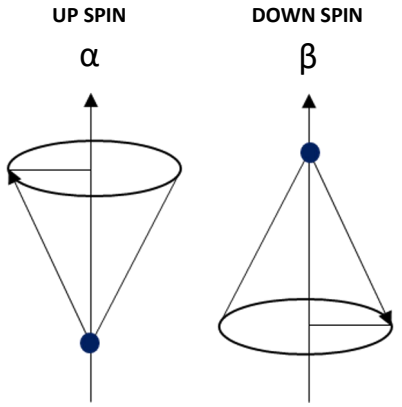

Figure 3. Vector model representation of electron spin, illustrating spin-up (α, left) and spin-down (β, right) states as precessing spin vectors around the vertical axis.

In the singlet state, the total spin angular momentum is zero ($S = 0$), and there is only one way to achieve this: the two spin vectors must be exactly antiparallel (see **Figure 4**). This configuration results in complete cancellation of the individual spin contributions, yielding no net spin vector. The corresponding spin wavefunction is an antisymmetric superposition of opposite spin states and is given by $\frac{1}{\sqrt{2}}(\alpha_1\beta_2 - \beta_1\alpha_2)$. In the triplet state, the total spin angular momentum is one ($S = 1$), and the two electron spins are aligned in a symmetric configuration. Unlike the singlet, the triplet state consists of three degenerate substates corresponding to different projections of the total spin along the z-axis. These are represented by the spin functions $\alpha_1\alpha_2$, $\frac{1}{\sqrt{2}}(\alpha_1\beta_2 + \beta_1\alpha_2)$, and $\beta_1\beta_2$, respectively. In the vector model, these configurations correspond to spin vectors that are either parallel or symmetrically arranged, resulting in a non-zero net spin vector (see **Figure 4**).

Device Note #1:

Electron–hole recombination in organic semiconductors obeys, under electrical injection i.e, organic light emitting diodes (OLEDs), simple spin statistics: 25 % of the generated excitons are *singlets* ($S = 0$) while the remaining 75 % are *triplets* ($S = 1$). .

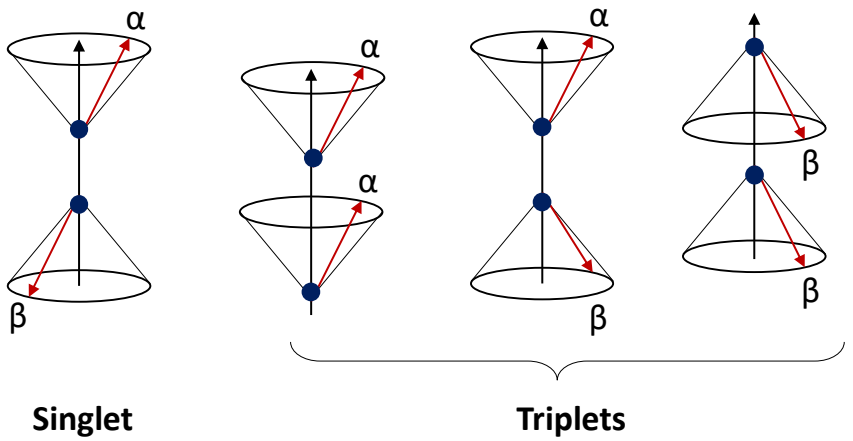

Figure 4. Vector model representations of spin configurations in singlet and triplet states. In the singlet state (left), the two electron spins are antiparallel ($\alpha\beta$), resulting in a net spin of zero. In the triplet states (right), electrons exhibit parallel or partially aligned spins ($\alpha\alpha$, $\alpha\beta$, or $\beta\beta$), leading to a net spin of one.

Potential energy surface

Each electronic state of a molecule, such as the ground state (S_0) and excited state (S_1), is associated with a unique potential energy surface (PES), which describes how the total energy of the system varies with the positions of the nuclei. This variation arises because the electronic distribution within a molecule determines the electrostatic forces acting on the nuclei. When a molecule undergoes an electronic transition (e.g., excitation from S_0 to S_1), the rearrangement of electrons alters these forces, resulting in a new PES with a different equilibrium geometry. Consequently, the nuclei adjust to a new set of positions that minimize the total energy under the new electronic configuration (see **Figure 5**). This is why the equilibrium nuclear positions, and thus the shape and minimum of the PES, differ from one electronic state to another. The PES framework is essential for understanding phenomena such as vibrational structure, absorption and emission spectra, and nonradiative transitions, all of which depend on the relationship between electronic and nuclear motion.

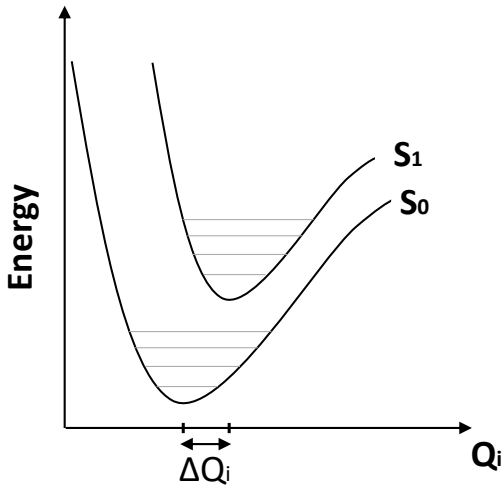

Figure 5. Configuration coordinate diagram illustrating the nuclei adjustment between S_0 and S_1.

1.1.4 Molecular transitions

Molecular transitions lie at the heart of photophysics and optoelectronic function: they convert the static quantum states described in the previous section into observable events such as absorption, fluorescence, phosphorescence, charge transfer, and non-radiative relaxation processes that dissipate energy without photon emission.

Radiative transitions

Whenever a molecule moves from one eigenstate Ψ_i to another Ψ_f, the process is governed by well-defined selection rules and rate laws that emerge from time-dependent perturbation theory. Central to this framework is **Fermi's Golden Rule**, which links the microscopic dipole–field interaction to a macroscopic transition rate through the squared matrix element $\left|\langle\Psi_f|\hat{H}'|\Psi_i\rangle\right|^2$ and the density of final states.

$$k_{if} \;=\; \frac{2\pi}{\hbar}\,\left|\langle\Psi_f|\hat{H}'|\Psi_i\rangle\right|^2 \rho(E_f), \tag{1}$$

where

k_{if} Transition rate from the initial state Ψ_i to the final state Ψ_f.

$\hbar$ Reduced Planck constant ($\hbar = h/2\pi$).

Ψ_i, Ψ_f Initial and final stationary eigenfunctions.

$\hat{H}'$ Perturbation Hamiltonian.

$\rho(E_f)$ Density of final states evaluated at the final energy E_f.

If we express the total molecular wavefunction as a product of the electronic, vibrational, and spin components:

$$\Psi_{\text{total}} = \Psi_{\text{el}} \cdot \Psi_{\text{vib}} \cdot \Psi_{\text{spin}}, \tag{2}$$

then the matrix element can be factorized accordingly, assuming these components are separable:

$$\left|\langle \Psi_f | \hat{H}' | \Psi_i \rangle\right|^2 = \left|\langle \Psi^f_{\text{el}} | \hat{e} \cdot \hat{r} | \Psi^i_{\text{el}} \rangle\right|^2 \cdot \left|\langle \Psi^f_{\text{vib}} | \Psi^i_{\text{vib}} \rangle\right|^2 \cdot \left|\langle \Psi^f_{\text{spin}} | \Psi^i_{\text{spin}} \rangle\right|^2 \tag{3}$$

Each term represents a different physical contribution to the transition probability, which can be described in detail below.

- **Electronic factor:**
  The first term,
  $$\left|\langle \Psi^f_{\text{el}} | \hat{e} \cdot \hat{r} | \Psi^i_{\text{el}} \rangle\right|^2,$$
  is the electronic transition dipole moment squared. It measures how strongly the electric dipole operator $\hat{e} \cdot \hat{r}$ couples the initial and final electronic states. This factor determines whether a transition is electronically allowed or forbidden based on orbital symmetry and overlap. It is directly related to experimentally measurable quantities such as oscillator strength and radiative lifetime. For instance, locally excited (LE) states with strong spatial overlap between the HOMO and LUMO generally exhibit higher oscillator strengths than charge-transfer (CT) states, where the HOMO and LUMO are spatially separated.

Device Note #2:

The oscillator strength f quantifies how strongly a molecule interacts with light at a given transition. In organic photodetectors (OPDs), a higher oscillator strength leads to stronger absorption at a given film thickness, thereby improving external quantum efficiency (EQE) and responsivity without requiring thick active layers that compromise charge extraction. In OLEDs, transitions with high oscillator strength produce narrowband emission with intense radiative rates, which enhances color purity and reduces excited-state lifetimes—both of which are critical for high-efficiency, low-rolloff displays. Conversely, transitions involving CT states often exhibit low oscillator strength, resulting in broader emission and reduced brightness unless compensated by device engineering.

- **Vibrational factor:**

  The second term,

$$\left| \langle \Psi^{f}_{\text{vib}} | \Psi^{i}_{\text{vib}} \rangle \right|^2 ,$$

  is the vibrational overlap, also known as the Franck–Condon factor. It quantifies the geometric overlap between the vibrational wavefunctions of the initial and final states, reflecting how the nuclei rearrange during the electronic transition. This means that electronic transitions in molecules occur so rapidly compared to nuclear motion that the nuclei are effectively frozen during the transition. As a result, the most probable transitions are vertical on a potential energy diagram, occurring between vibrational levels of the ground and excited electronic states that have significant spatial wavefunction overlap. This principle governs both absorption and emission processes: absorption typically excites the molecule from the vibrational ground state of S_0 to multiple vibrational levels of S_1, while emission (e.g., fluorescence) occurs from the lowest vibrational level of S_1 down to various vibrational levels of S_0 as illustrated in **Figure 6**. The distribution of these vibrational transitions leads to the characteristic broadening of molecular absorption and emission spectra, with the width and shape determined by the extent of nuclear displacement between the initial and final states. Molecules with large geometry changes upon excitation exhibit broader spectra due to a wider spread of Franck–Condon-active transitions, whereas rigid molecules with minimal structural reorganization tend to produce narrower spectral features.

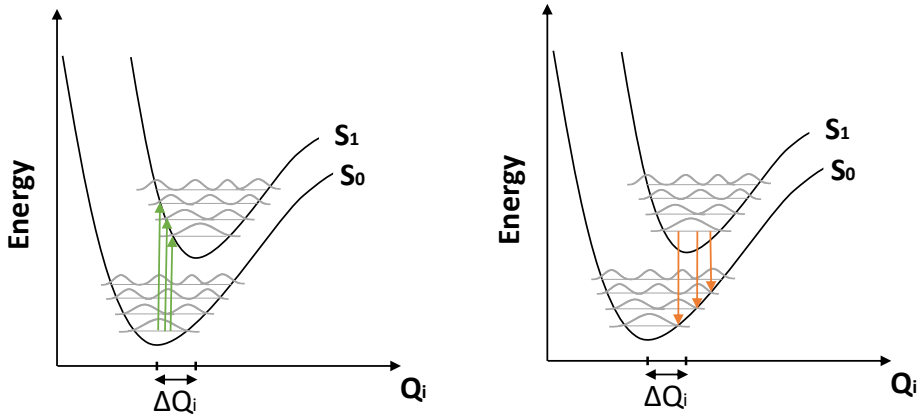

Figure 6. Visualization of the Franck–Condon principle using simplified potential energy surfaces along a single normal mode. The left diagram illustrates the absorption process (green arrows). The right diagram depicts the emission process (orange arrows).

Device Note #3:

Most organic semiconductors exhibit broad absorption profiles as a result of vibronic coupling, conformational flexibility, and molecular disorder. Achieving sharp, isolated spectral features typically requires highly rigid and symmetric molecular architectures. However, such systems often suffer from synthetic complexity, poor solubility, and limited environmental stability. These challenges constrain the broader application of organic semiconductors in narrowband OPD technologies, where spectral selectivity and material processability must be simultaneously optimized.

- **Spin factor:**

  The third term,

$$\left|\langle \Psi^{f}_{\text{spin}} | \Psi^{i}_{\text{spin}} \rangle\right|^2,$$

  encodes the spin selection rules. It determines whether the transition conserves spin angular momentum. For example, transitions between states with the same total spin (e.g., singlet to singlet or triplet to triplet) are typically spin-allowed, while transitions involving a change in spin multiplicity (e.g., singlet to triplet) are spin-forbidden unless spin–orbit coupling is significant (see **Figure 7**). This factor is especially important in distinguishing fluorescence from phosphorescence and governs intersystem crossing rates. However, when spin–orbit coupling is included in the electronic Hamiltonian, the nominally pure singlet and triplet eigenstates acquire small admixtures of each other's spin character. As a result, the true excited-state wavefunctions can be written approximately as

$$\Psi'_{S_1} \approx \Psi_{S_1} + \lambda\, \Psi_{T_m}, \quad \Psi'_{T_1} \approx \Psi_{T_1} + \lambda\, \Psi_{S_n},$$

  where λ is proportional to the spin–orbit coupling strength and Ψ_{T_m}, Ψ_{S_n} are triplet and singlet basis states of appropriate symmetry. This mixing breaks the strict spin-selection rule, allowing otherwise forbidden transitions, such as intersystem crossing ($S_1 \rightarrow T_1$) and phosphorescence ($T_1 \rightarrow S_0$), to occur with finite, albeit slow, rates.

Device Note #4:

Fluorescent emitters rely on spin-allowed transitions from the singlet excited state (S_1) to the singlet ground state (S_0), governed by the spin-selection rule $\Delta S = 0$. Consequently, triplet excitons generated during electrical excitation (75% by spin statistics) remain non-emissive and undergo non-radiative decay, capping the internal quantum efficiency (IQE) at 25%. In contrast, phosphorescent emitters incorporate heavy-atom complexes to enhance spin–orbit coupling, enabling otherwise spin-forbidden $T_1 \rightarrow S_0$ transitions and harvesting triplet excitons for radiative decay. This allows phosphorescent OLEDs to achieve IQEs approaching 100%.

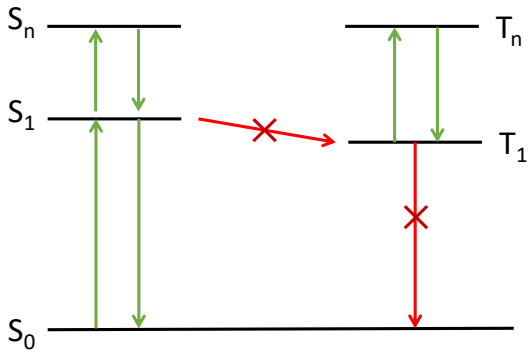

Figure 7. Schematic energy-level diagram illustrating spin-allowed and spin-forbidden transitions. Green arrows denote spin-allowed absorption and emission between singlet states ($S_0 \leftrightarrow S_1 \leftrightarrow S_n$) and between triplet states ($T_1 \leftrightarrow T_n$). The red arrow with an "$\times$" indicates the spin-forbidden intersystem crossing ($S_1 \rightarrow T_1$) and phosphorescence ($T_1 \rightarrow S_0$) pathways, which are weak in the absence of spin–orbit coupling.

Non-radiative transitions

Non-radiative transitions are processes in which a molecule relaxes from a higher electronic state to a lower one by releasing energy as heat, rather than emitting a photon. This energy dissipation occurs through molecular vibrations. There are two primary non-radiative pathways: internal conversion (IC) and intersystem crossing (ISC). IC occurs when the molecule transitions between two electronic states of the same spin multiplicity (e.g., $S_1 \rightarrow S_0$). In contrast, ISC involves a transition between states of different spin multiplicities (e.g., $S_1 \rightarrow T_1$). Although spin-forbidden by selection rules, ISC is enabled by spin–orbit coupling, which facilitates the process by allowing spin flipping during the transition.

It is important to note that non-radiative transitions are *isoenergetic* because they occur between two vibrational levels of different electronic states that possess the same energy. Such transitions are typically represented by a horizontal arrow, in contrast to radiative transitions, which are depicted by vertical arrows. Non-radiative transitions are usually followed by rapid and irreversible thermal relaxation as shown in **Figure 8**).

Device Note #5:

In contrast to fluorescent emitters, TADF molecules employ reverse intersystem crossing (RISC) to thermally up-convert non-emissive triplet excitons into the singlet manifold ($T_1 \rightarrow S_1$), a process enabled by a small singlet–triplet energy gap (ΔE_{ST}) and enhanced spin-orbit coupling. This mechanism allows the harvested triplets to undergo spin-allowed $S_1 \rightarrow S_0$ fluorescence, effectively raising the IQE limit to nearly 100% in OLEDs.

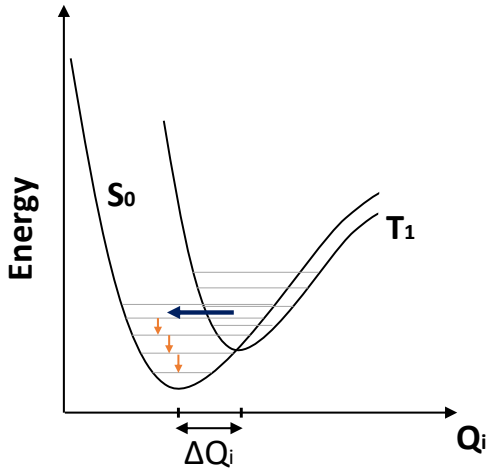

Figure 8. Potential energy diagram illustrating non-radiative transition (blue arrow), followed by rapid thermal relaxation (orange arrows) to the S_0 equilibrium geometry.

Similar to radiative transitions, Fermi's Golden Rule provides a general expression for the rate of a non-radiative transition:

$$k_{\mathrm{nr}} = \frac{2\pi}{\hbar} \left| \langle \Psi_f | \hat{H}' | \Psi_i \rangle \right|^2 \rho(E_f), \tag{4}$$

where the perturbing Hamiltonian $\hat{H}'$ responsible for inducing the radiationless transition is given by the nuclear kinetic energy operator $\partial/\partial Q$ and the total matrix element can be factorized into electronic, vibrational, and spin contributions by writing the total wavefunction as $\Psi = \Psi_{\mathrm{el}}\Psi_{\mathrm{vib}}\Psi_{\mathrm{spin}}$:

$$\left| \langle \Psi_f | \hat{H}' | \Psi_i \rangle \right|^2 = |J|^2 FS, \tag{5}$$

with $J = \langle \Psi^f_{\mathrm{el}} | \hat{H}' | \Psi^i_{\mathrm{el}} \rangle$ representing the electronic coupling between the two states,

$$F = \left| \langle \Psi^f_{\mathrm{vib}} | \Psi^i_{\mathrm{vib}} \rangle \right|^2 \tag{6}$$

denoting the Franck–Condon factor (vibrational overlap), and

$$S = \left| \langle \Psi^f_{\mathrm{spin}} | \Psi^i_{\mathrm{spin}} \rangle \right|^2 \tag{7}$$

representing the spin overlap. The spin factor S equals 1 for transitions within the same spin manifold (e.g., internal conversion) but can be very small for spin-forbidden processes (e.g., intersystem crossing) unless enhanced by spin–orbit coupling.

Because the vibrational overlap decreases exponentially with the energy gap ΔE between the two electronic states,

$$F \propto \exp\left(-\frac{\Delta E}{\hbar\omega}\right), \tag{8}$$

substitution into Eq. 1 leads directly to the energy gap law:

$$k_{\mathrm{nr}} \propto |J|^2 S \exp\left(-\frac{\Delta E}{\hbar\omega}\right). \tag{9}$$

This relation shows that a large energy gap results in a small Franck–Condon factor and a slow non-radiative decay rate, whereas a small energy gap yields a larger vibrational overlap and thus a faster non-radiative transition.

Device Note #6:

The energy gap law has significant implications for near-infrared (NIR) optoelectronic devices. As the energy gap ΔE decreases to access longer wavelengths, the Franck–Condon overlap F between the vibrational wavefunctions of the initial and final states increases, which exponentially enhances the non-radiative decay rate k_{nr}. This enhanced non-radiative loss quenches photoluminescence in NIR emitters and shortens excited-state lifetimes, directly lowering the EQE in OLEDs and the photoluminescence quantum yield (PLQY) in emissive materials. Similarly, for NIR photodetectors, the energy gap law increases non-radiative recombination, elevating dark current and reducing detectivity.

1.1.5 Energy transfer

Similar to intramolecular transitions, where energy is exchanged within the same molecule, energy can also be transferred between different molecules. In this case, if the excitation is transferred in an incoherent manner from one molecule, referred to as the energy donor (D), to another molecule, called the energy acceptor (A), the process is known as intermolecular energy transfer. This transfer can occur through either a radiative or a non-radiative mechanism.

In the radiative pathway, the donor emits a photon, which is subsequently absorbed by the acceptor in a two-step process, provided there is sufficient spectral overlap between the donor's emission and the acceptor's absorption. This radiative energy transfer is a long-range process and does not require direct quantum chemical coupling between D and A.

By contrast, non-radiative energy transfer is a one-step process in which the donor is de-excited and the acceptor is simultaneously excited through a coupling interaction. This mechanism typically requires close proximity between D and A and is strongly dependent on their electronic coupling.

Förster and Dexter energy transfer

Förster energy transfer (FRET): FRET is a long-range, non-radiative dipole–dipole coupling mechanism in which excitation energy is transferred from a donor (D) molecule in an excited electronic state to an acceptor (A) molecule in a lower-energy state (see **Figure 9a**). This process does not involve photon emission; instead, the donor's excitation energy is directly transferred to the acceptor.

FRET is highly sensitive to the donor–acceptor separation distance and is effective in the 1–10 nm range. The transfer rate is given by:

$$k_{\mathrm{DA}} = \frac{1}{\tau_D}\left(\frac{R_0}{R}\right)^6, \tag{10}$$

where τ_D is the donor's lifetime in the absence of an acceptor, R is the donor–acceptor distance, and R_0 is the Förster radius (the distance at which the transfer efficiency is 50%).

The Förster radius depends on the orientation factor κ^2, the refractive index n of the medium, and the spectral overlap integral J:

$$R_0 = \left[8.8 \times 10^{17} \frac{\kappa^2}{n^4} \int g_A(E) g_D(E) dE\right]^{1/6}, \tag{11}$$

where $g_D(E)$ and $g_A(E)$ are the normalized donor emission and acceptor absorption spectra, respectively. FRET requires significant spectral overlap but does not require direct orbital overlap between D and A.

Dexter energy transfer (DET): DET is a short-range electron-exchange mechanism that requires direct orbital overlap between the donor and acceptor molecules. Energy transfer occurs through a two-electron exchange process in which one electron is transferred from the LUMO of the donor to the LUMO of the acceptor while another electron simultaneously moves from the HOMO of the acceptor to the HOMO of the donor (see **Figure 9b**).

Because Dexter transfer requires wavefunction overlap, it is only effective at very short distances (0.5–2 nm). The transfer rate decays exponentially with distance:

$$k_{\mathrm{Dexter}} = J^2 \beta^2 \exp\left(-\frac{2R}{L}\right), \tag{12}$$

where J is the electronic coupling, R is the donor–acceptor separation distance, and L is the decay constant of the orbital wavefunction. Unlike FRET, Dexter transfer can mediate both singlet and triplet energy transfer.

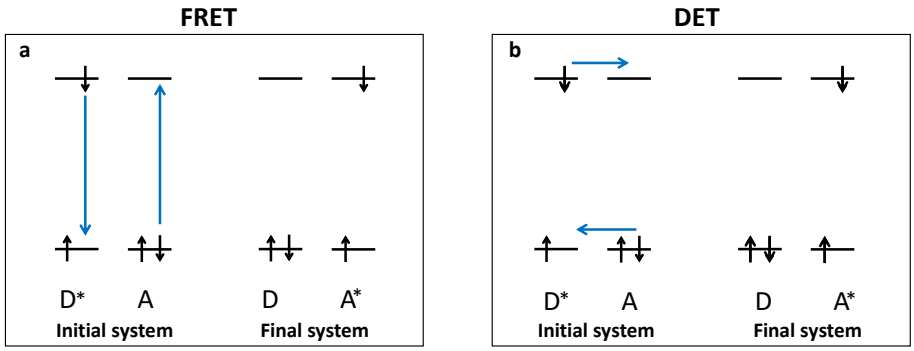

Figure 9. Schematic of resonant energy transfer mechanisms: (a) long-range Förster transfer via Coulombic dipole–dipole coupling, and (b) short-range Dexter transfer via electron exchange coupling.

1.2 Light–matter interaction

Light–matter interaction is a core principle in physics and chemistry, describing how electromagnetic radiation and materials mutually affect each other. This interaction can result in absorption, transmission, reflection, or scattering of light, transferring energy to excite atoms or molecules and induce changes. Crucially, the strength of this coupling can be tailored by altering the electromagnetic environment, using cavities or nanostructures to enhance or suppress it.

1.2.1 Optical microcavities

As suggested by their name, *(micro)*cavities are compact optical resonators whose dimensions are comparable to the wavelength of light. They serve the purpose of confining electromagnetic fields within a highly restricted volume. Among the various designs, Fabry–Pérot cavities represent the most widely utilized form of microcavities, particularly in the field of organic optoelectronics. This type of cavity consists of two highly reflective, parallel mirrors separated by a spacer layer whose thickness is typically on the order of a micrometer or less. In practical implementations, at least one of the mirrors is semi-transparent, enabling photons to both enter and exit the cavity.

The resonance condition of the cavity is satisfied when the optical path length of the cavity corresponds to an integer multiple of half the wavelength of the confined light. This condition gives rise to the formation of a standing wave perpendicular to the mirror surfaces, and the corresponding resonant wavelength, λ, is given by

$$\lambda = \frac{2n_c d_c}{m}, \tag{13}$$

where n_c is the effective refractive index of the cavity, d_c is the physical thickness of the spacer layer, and $m \geq 1$ is an integer representing the cavity mode order. It is evident from Equation 13 that the resonant wavelength can be tuned by adjusting either the cavity thickness or the refractive index of the spacer layer.

For convenience, the resonance condition may alternatively be expressed in terms of the wavevector, k, defined as

$$k = \frac{2\pi}{\lambda}, \tag{14}$$

which relates the wavelength of the confined optical mode to its spatial frequency. These expressions illustrate that the optical properties of Fabry–Pérot microcavities can be readily controlled through precise manipulation of their geometrical and material parameters.

The optical wavevector k of light confined within a Fabry–Pérot microcavity can be decomposed into two orthogonal components: one perpendicular ($k_\perp$) and one parallel ($k_\parallel$) to the cavity mirrors. This decomposition is expressed as

$$k^2 = k_\perp^2 + k_\parallel^2, \tag{15}$$

where $k_\perp$ is the component along the cavity normal and $k_\parallel$ is the in-plane component. For an internal propagation angle θ_i (relative to the cavity normal), the perpendicular component is given by

$$k_\perp = k \cos\theta_i. \tag{16}$$

The Fabry–Pérot resonance condition requires that the optical path length in the perpendicular direction is an integer multiple of half the wavelength. This condition is written as

$$k_\perp = \frac{\pi m}{n_c d_c}, \tag{17}$$

where $m \geq 1$ is the longitudinal cavity mode order, n_c is the effective refractive index, and d_c is the spacer layer thickness. The parallel component can similarly be expressed as

$$k_\parallel = \frac{\pi m \tan\theta_i}{n_c d_c}. \tag{18}$$

Combining these expressions yields the angle-dependent resonant wavelength

$$\lambda_\theta = \frac{2 n_c d_c \cos\theta_i}{m}. \tag{19}$$

Equation 19 demonstrates that as the internal viewing angle θ_i increases, the factor $\cos\theta_i$ decreases, resulting in a shorter resonant wavelength.

The energy of the cavity mode at angle θ_i is obtained from $E = hc/\lambda_\theta$, leading to

$$E_\theta = \frac{E_0}{\cos\theta_i}, \tag{20}$$

where $E_0 = hc/(2n_c d_c)$ is the cavity mode energy at normal incidence ($\theta_i = 0$). Equation 20 shows that the mode energy increases as the viewing angle increases.

In practice, the cavity is observed from outside the medium, so the internal angle θ_i must be related to the external viewing angle θ_{ext}. Using Snell's law,

$$n_a \sin\theta_{\text{ext}} = n_c \sin\theta_i, \tag{21}$$

where n_a is the refractive index outside the cavity (typically air, $n_a = 1$). Substituting into Equation 20, the energy can be expressed directly in terms of the external viewing angle as

$$E_{\text{ext}} = \frac{E_0}{\sqrt{1 - \frac{\sin^2\theta_{\text{ext}}}{n_c^2}}}. \tag{22}$$

Equation 22 describes the angular dispersion of the cavity mode as observed externally: as the viewing angle θ_{ext} increases, E_{ext} increases and the corresponding resonant wavelength decreases.

These relations demonstrate that the resonant wavelength and energy of Fabry–Pérot microcavities are not only determined by their thickness and refractive index but also by the propagation angle of light within the cavity. At normal incidence ($\theta_{\text{ext}} = 0$), the mode energy is E_0. As the viewing angle increases, the optical path length inside the cavity effectively decreases, leading to a higher resonant energy and shorter wavelength. This angular dependence is crucial for understanding the dispersion characteristics of microcavity modes.

Device Note #7:

Employing optical cavities is a highly effective strategy for achieving narrowband emission or absorption in organic optoelectronic devices such as OLEDs and OPDs. The resonance of the cavity selectively enhances specific optical modes, leading to sharp spectral profiles that are otherwise difficult to obtain with organic semiconductors alone. However, a key limitation of cavity-based approaches is their inherent angular dispersion: the resonance wavelength shifts with the emission or incidence angle. This angular dependence can be problematic for applications that require angle-independent operation, such as wide-viewing-angle displays or omnidirectional photodetectors.

1.2.2 Weak light–matter interaction

In the weak coupling regime, the interaction strength g between light and matter is much smaller than the cavity loss rate κ and the emitter decay rate γ, i.e. $g \ll$

(κ, γ). In this case, the exchange of energy between the emitter and the cavity field is irreversible, meaning that any photon emitted into the cavity mode will escape or be absorbed before it can be reabsorbed by the emitter. As a result, the electromagnetic field and the emitter quickly dephase and the coupling can be treated perturbatively.

This perturbative regime allows the spontaneous emission rate of the emitter to be engineered by modifying the local density of optical states (LDOS) through cavity design. If the electronic transition is spectrally resonant with the cavity mode, the spontaneous emission rate is enhanced; if it is detuned, the emission is suppressed. This phenomenon is known as the Purcell effect. The enhancement is quantified by the Purcell factor, F_P, which is expressed as

$$F_P = \frac{3}{4\pi^2}\left(\frac{\lambda_c}{n_{\text{eff}}}\right)^3 \frac{Q}{V_{\text{eff}}}, \tag{23}$$

where λ_c is the cavity resonant wavelength, n_{eff} is the effective refractive index of the cavity, Q is the quality factor, and V_{eff} is the effective optical mode volume. A large Q (low losses) and a small V_{eff} (high confinement) maximize the Purcell enhancement.

The Purcell factor represents the ratio of the spontaneous emission rate in the presence of the cavity to that in free space. More formally, this relationship is described by Fermi's golden rule mentioned earlier. Equation 1 shows that the emission rate can be increased by enhancing the density of states $\rho\big(E_f\big)$ available for the emitter, which is exactly what a well-designed microcavity accomplishes.

It is important to note that the Purcell factor given in Equation 23 corresponds to the maximum achievable enhancement under ideal conditions, i.e. when the emitter is perfectly resonant with the cavity mode, the dipole moment is aligned with the electric field, and all transitions are purely radiative. Deviations from these ideal conditions, such as detuning, misalignment, or non-radiative losses, reduce the observed enhancement.

Device Note #8:

The ability to control spontaneous emission through weak optical coupling is fundamental in the design of organic optoelectronic devices such as lasers and narrowband light-emitting diodes. In these devices, precise spectral control and the ability to achieve low lasing thresholds are critical for efficient and high-performance operation.

1.2.3 Strong light–matter interaction

In the strong coupling regime, the light–matter interaction strength exceeds both the cavity photon decay rate and the matter dephasing rate, such that $g \gg (\kappa, \gamma)$. Under these conditions, energy is exchanged coherently and reversibly between the cavity field and the matter at a rate defined by the Rabi frequency, Ω. This coherent

interaction results in the formation of new hybrid eigenstates of the system known as *polaritons*, which are part-light and part-matter quasiparticles (**Figure 10**).

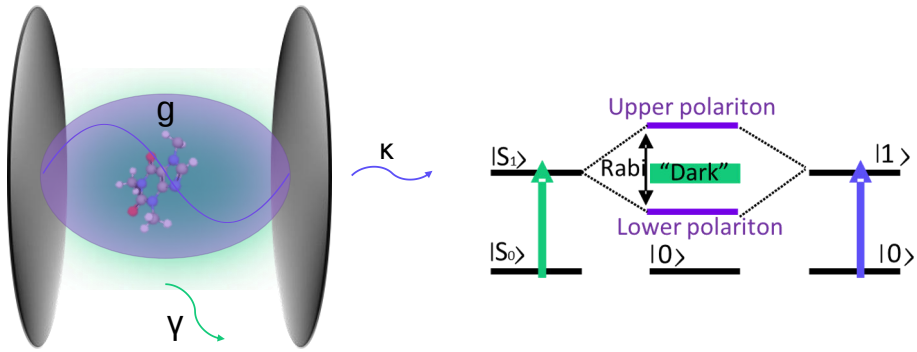

Figure 10. Strong light–matter coupling in a Fabry–Pérot cavity. Left: a molecular ensemble couples to a single cavity mode with strength g; κ and γ denote the cavity and molecular loss rates, respectively. Right: the bare exciton $|S_1\rangle$ and the cavity photon hybridize into lower and upper polaritons separated by the Rabi splitting, while a manifold of dark states remains near the exciton energy.

From a quantum electrodynamical perspective, this phenomenon arises due to the interaction of matter with the quantized vacuum field. Even in the absence of external photons, the cavity contains fluctuating electromagnetic fields, referred to as vacuum fluctuations or zero-point energy. These fluctuations represent the ground-state energy of the quantized electromagnetic field and originate from the Heisenberg uncertainty principle, which prohibits the simultaneous vanishing of the electric and magnetic field energies. In optical cavities, the strength of the vacuum electric field is enhanced due to mode confinement and is given by

$$\mathcal{E}_{\mathrm{vac}} = \sqrt{\frac{\hbar\omega_c}{2\varepsilon_0 V}},$$

where ω_c is the cavity resonance frequency, ε_0 is the vacuum permittivity, and V is the effective mode volume. [4]

The interaction between a two-level molecular system and a single mode of the quantized electromagnetic field is commonly described by the Jaynes–Cummings model [5]. In this framework, the total Hamiltonian is expressed as the sum of three contributions:

$$\hat{H}_{\mathrm{JC}} = \hat{H}_{\mathrm{mol}} + \hat{H}_{\mathrm{field}} + \hat{H}_{\mathrm{int}},$$

where $\hat{H}_{\mathrm{mol}}$ describes the two-level molecule with specific transition frequency ω_x, $\hat{H}_{\mathrm{field}}$ represents the cavity mode of frequency ω_c, and $\hat{H}_{\mathrm{int}}$ accounts for the light–matter interaction, with g as the coupling strength.

Diagonalizing this Hamiltonian yields two new eigenstates, known as the upper and lower polariton states, which are coherent superpositions of the uncoupled basis states $|e,0\rangle$ (excited molecule, no photon) and $|g,1\rangle$ (ground-state molecule, one photon):

$$|P^+\rangle = \alpha|e,0\rangle + \beta|g,1\rangle, \qquad |P^-\rangle = \beta|e,0\rangle - \alpha|g,1\rangle,$$

the coefficients α and β are the mixing coefficients that determine the photonic and excitonic character of the polaritonic states, also called Hoppfield coefficients. These coefficients depend on the detuning $\Delta = \omega_x - \omega_c$ between the molecular and cavity resonance frequencies and the coupling strength g. These polaritonic eigenstates represent the hybridization of light and matter and are separated in energy by the vacuum Rabi splitting $\Omega_R = 2g$ at zero detuning ($\omega_x = \omega_c$), which serves as the signature of the strong coupling regime as illustrated in **Figure 11**.

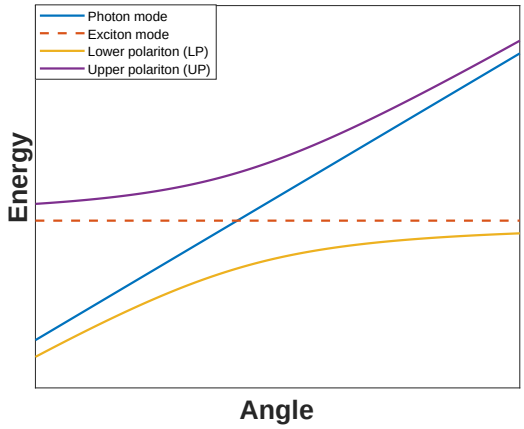

Figure 11. Angle-resolved dispersion showing a flat exciton mode (dashed) and a dispersive cavity photon mode (blue), which hybridize under strong coupling to form the lower (LP, gold) and upper (UP, purple) polariton branches, illustrating the avoided crossing characteristic of polaritons.

The cavity detuning is defined as negative when the cavity resonance frequency is lower than the molecular transition frequency ($\omega_x > \omega_c$), and as positive when it is higher ($\omega_x < \omega_c$).

The Rabi splitting is defined as the energy difference between the upper and lower polariton branches in resonance and is expressed as

$$\hbar\Omega_R = 2\hbar g = 2d\sqrt{N}\sqrt{\frac{\hbar\omega_c}{2\varepsilon_0\mathcal{V}}},$$

where Ω_R is the Rabi frequency, d is the transition dipole moment, N is the number of coherently coupled molecules, ω_c is the cavity resonance frequency, ε_0 is the vacuum permittivity, and $\mathcal{V}$ is the effective mode volume of the cavity.

Due to their photonic component, polaritons exhibit angular dispersion similar to that of cavity photons, as described in Equation 19. However, because polaritons are hybrid light–matter quasiparticles, formed from a coherent superposition of excitonic and photonic states, their dispersion is governed by the mixing coefficients α and β, which represent the photonic and excitonic contributions, respectively.

At zero detuning ($\Delta = 0$), the polaritons are maximally hybridized, with $\alpha = \beta$, resulting in both upper and lower polariton branches sharing equal photonic and excitonic character. In this case, the lower polariton exhibits noticeable angular dispersion due to its significant photonic content. As the detuning becomes strongly positive (blue-detuned), the lower polariton becomes more excitonic and its dispersion flattens, while the upper polariton becomes more photonic and inherits the full dispersion of the cavity mode. Conversely, under strong negative (red) detuning, the lower polariton becomes more photonic and the upper polariton more excitonic. Thus, by tuning the detuning Δ, one can effectively modulate the angular dispersion and energy curvature of the polariton branches as shown in **Figure 12** [4].

Polariton population

Polaritons can be populated via two primary pathways: vibrational relaxation and radiative pumping. In the former, population transfers from the exciton reservoir to the polariton branches through nonradiative relaxation accompanied by the emission of one or more phonons. In the latter, spontaneous emission from the incoherent exciton manifold couples to the cavity mode and feeds the polariton states (radiative pumping). A significant spectral overlap between the exciton emission and the polariton mode renders radiative pumping particularly efficient [6].

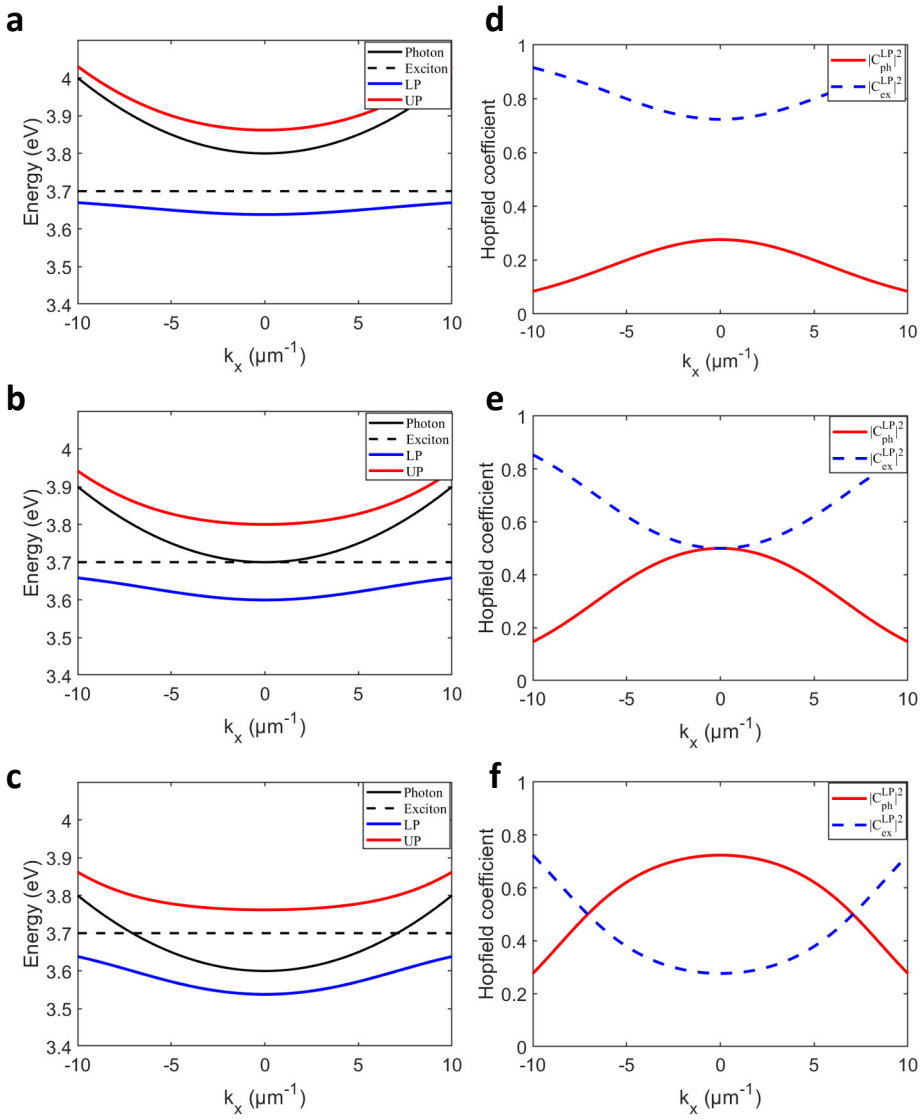

Figure 12. Polariton dispersion relations and Hopfield coefficients at different detunings. (a–c) Calculated dispersions of the upper (UP, red) and lower (LP, blue) polariton branches for (a) positive, (b) zero, and (c) negative detunings. The black solid line is the bare cavity photon dispersion and the black dashed line marks the exciton energy. (d–f) Corresponding LP Hopfield coefficients showing the photonic and excitonic fractions, $|C_{\mathrm{ph}}^{\mathrm{LP}}|^2$ (red) and $|C_{\mathrm{ex}}^{\mathrm{LP}}|^2$ (blue), as functions of in-plane wavevector k_x, highlighting the evolution from photon-like (negative detuning) to exciton-like (positive detuning) character.

1.3 Organic optoelectronics

Organic optoelectronics is an interdisciplinary field that utilizes the electronic and optical properties of organic semiconductors to enable a broad range of light-based technologies. Organic optoelectronic devices, including OLEDs, OPDs, and organic solar cells (OSCs), have emerged as promising alternatives to their inorganic counterparts in applications such as displays, lighting, and low-cost sensing. In this thesis, OLED and OPD devices were developed; therefore, the following section provides an overview and a brief introduction to the operating principles of these two device types.

1.3.1 Organic light-emitting diodes

OLEDs have emerged as a cornerstone technology in modern optoelectronics, widely used in smartphones, televisions, wearable displays, and emerging flexible lighting applications. Their popularity stems from their thin form factor, high contrast ratios, low power consumption, and capability for flexible and transparent device architectures.

Working principle

A typical OLED consists of multiple organic semiconductor layers sandwiched between two electrodes. These layers are responsible for injecting, transporting, and recombining charge carriers to produce light through the process of electroluminescence. The structure and operation of OLEDs can be divided into two key aspects: the device architecture and the carrier dynamics.

A conventional OLED is composed of the following layers (see **Figure 13a**):

- **Anode:** Typically indium tin oxide (ITO), which is transparent and has a high work function to facilitate hole injection.
- **Hole Transport Layer (HTL):** Assists holes in reaching the emissive layer.
- **Emissive layer (EML):** The active layer where electrons and holes recombine and emit photons.
- **Electron transport layer (ETL):** Helps electrons move efficiently toward the EML.
- **Cathode:** Often a low work function metal like Ca/Ag, enabling efficient electron injection.

Optional layers such as hole injection layers (HIL) and electron blocking layers (EIL) may also be incorporated to optimize injection and recombination efficiency.

The OLED operation can be described in three main steps:

Step 1: Carrier injection: When a forward bias is applied, holes are injected from the anode into the HOMO levels of the HTL/EIL, while electrons are injected from the cathode into the LUMO levels of the ETL/HIL.

Step 2: Carrier transport: The injected carriers are transported through the respective transport layers. The electron transport materials typically exhibit LUMO energy levels that are close to those of the EML, while the hole transport materials have HOMO levels aligned similarly with the EML, as illustrated in **Figure 13b**. Significant energy mismatches between the EML and the transport layers can lead to undesirable outcomes such as energy losses or charge injection barriers. To mitigate charge leakage from the EML without exciton formation, the ETL is generally designed with a shallower LUMO, and the HTL with a deeper HOMO, relative to the EML.

Step 3: Exciton formation and emission: At the EML, electrons and holes recombine to form excitons. These excitons decay radiatively, emitting photons in a process known as electroluminescence. This light emission is current-driven and is the core principle of OLED operation.

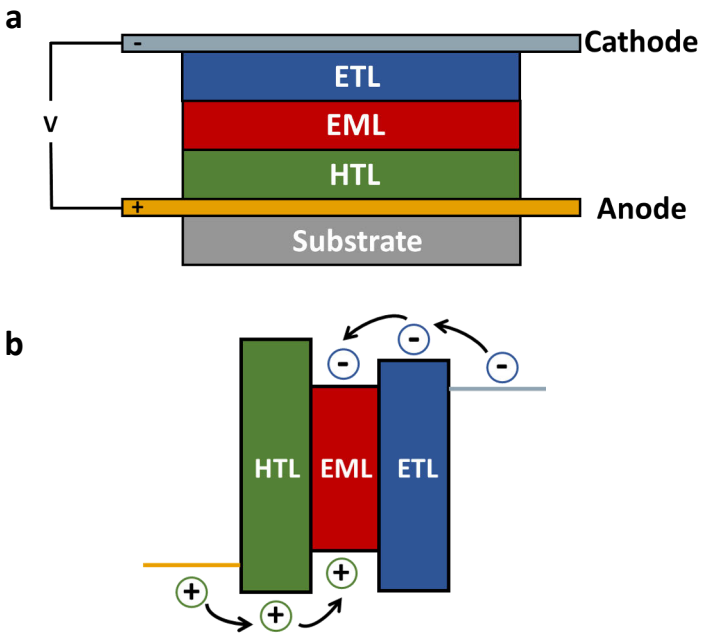

Figure 13. (a) Layered architecture of a bottom-emitting OLED on a substrate, showing anode/HTL/EML/ETL/cathode with the polarity of the applied bias V. (b) Simplified operating scheme: holes are injected from the anode into the HTL and electrons from the cathode into the ETL; carriers drift/diffuse toward the EML where they recombine to form excitons that emit light.

Material systems for OLEDs

Two material systems are being developed commercially for OLEDs to achieve high efficiency and color purity. Conventional fluorescent emitters (FEs) are primarily employed in the fabrication of blue OLEDs, whereas phosphorescent emitters (PEs) are utilized for green and red OLEDs. In FE-based OLEDs, as disscussed in section 1.1, spin statistics limit the IQE to 25% under electrical excitation, as only singlet excitons contribute to photon emission. Consequently, significant efforts have been made to harness the long-lived triplet excitons. One viable strategy involves incorporating rare metal complexes into the organic framework to enhance spin-orbit coupling between S_1 and T_1 states in PEs. This enables harvesting excitons from both spin states, pushing the IQE close to 100%. However, these rare metal complexes pose environmental concerns.

Recently, purely organic emitters have been developed to achieve efficient upconversion of triplets to singlets via the thermally activated delayed fluorescence (TADF) mechanism. TADF-based OLEDs offer the potential to reach 100% IQE through a triplet harvesting process that avoids the use of heavy metals. In TADF emitters, triplets can be harvested through RISC by minimizing the singlet-triplet energy gap (ΔE_{ST}). **Figure 14** schematically compares the exciton utilization mechanisms in fluorescent, phosphorescent, and TADF emitters.

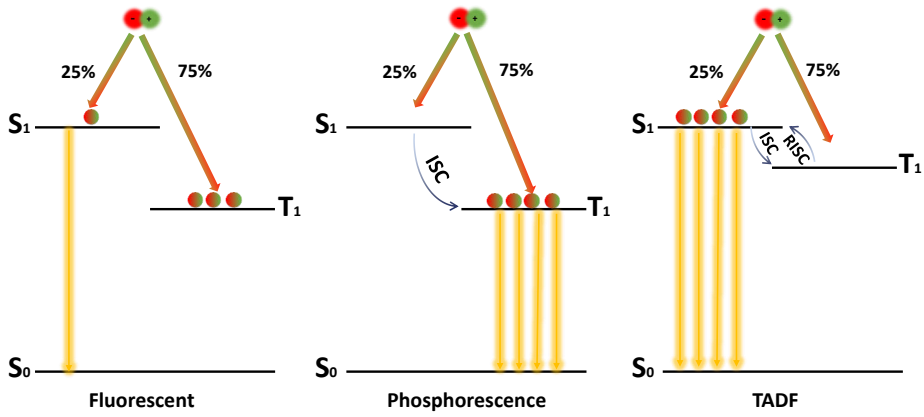

Figure 14. Electroluminescence pathways in OLEDs under spin statistics (25% singlets, 75% triplets). **Left:** Fluorescent emitter, only singlet excitons decay radiatively ($S_1 \rightarrow S_0$), while triplets are lost non-radiatively. **Middle:** Phosphorescent emitter, enhanced spin–orbit coupling enables ISC to T_1 and radiative phosphorescence ($T_1 \rightarrow S_0$), harvesting triplets. **Right:** TADF emitter, a small ΔE_{ST} allows RISC from T_1 to S_1; emission occurs as prompt and delayed fluorescence from S_1, enabling efficient triplet harvesting without heavy metals.

1.3.2 Organic photodiodes

OPDs have gained significant attention in recent years due to their potential for lightweight, flexible, and low-cost optical sensing technologies. They are increasingly being integrated into real-world applications such as biometric authentication (e.g., fingerprint and pulse oximetry sensors), environmental monitoring, image sensing, and wearable electronics, where their mechanical flexibility and spectral tunability offer distinct advantages over traditional inorganic photodetectors.

Operation principles

A conventional OPD typically consists of a multilayer structure comprising an anode, an HTL, an active photoactive layer (donor–acceptor blend), an ETL, and a cathode. OPDs generally operate under reverse bias, enhancing the separation and collection of photo-generated charge carriers. **Figure 15** schematically summarizes the operating principle of a donor–acceptor OPD, highlighting carrier generation at the D/A interface and their selective transport to the anode (holes via HTL) and cathode (electrons via ETL).

The working principle of OPDs relies on three main processes:

- **Photon absorption and exciton generation:** When light is absorbed in the photoactive layer, it generates bound electron-hole pairs called excitons. This process typically occurs in the donor or acceptor domains, depending on the absorption characteristics.
- **Exciton diffusion and dissociation:** The excitons diffuse towards the donor–acceptor interface. Due to the energy level offset at the heterojunction, the excitons dissociate into free charge carriers—electrons and holes—which are then separated into the acceptor and donor phases, respectively.
- **Charge transport and collection:** The separated charges are transported through the ETL and HTL to their respective electrodes. The built-in electric field in the device, enhanced by the applied reverse bias, aids the drift and diffusion of carriers toward the electrodes, where they are collected as photocurrent.

The performance of an OPD is determined by parameters such as EQE, responsivity, specific detectivity (D^*), and dark current. Optimizing layer energetics and morphology is essential to enhance exciton dissociation efficiency, reduce recombination losses, and improve overall device sensitivity and speed.

1.3.3 Polaritons for organic optoelectronics

As outlined in Section 1.2.3, polaritons arise from the strong coupling between molecular excitations and optical cavity modes. Organic materials serve as an ex-

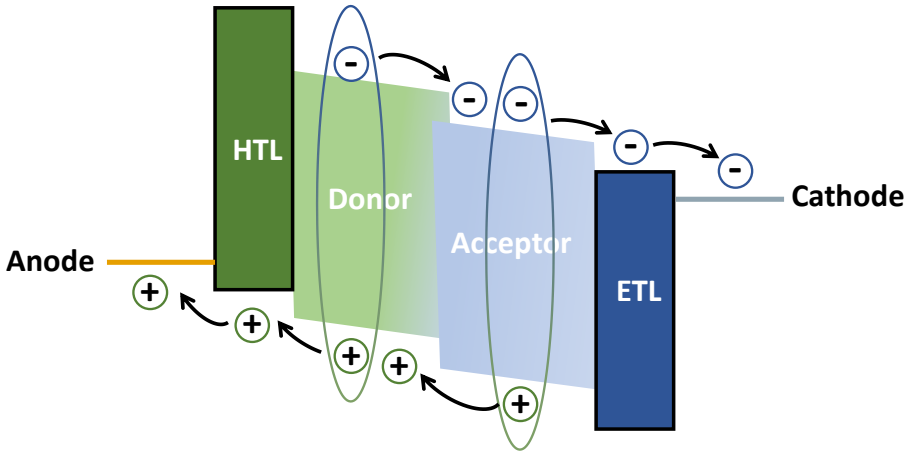

Figure 15. Schematic energy/transport diagram of a donor–acceptor organic photodiode.

cellent platform for supporting polaritons due to the high binding energy of Frenkel excitons, which are the primary excitations in organic molecular systems. Polaritons formed within organic materials, referred to as organic polaritons, hold significant promise for advancing efficient organic optoelectronic devices, thanks to their unique hybrid light–matter properties. In this section, key properties of polaritons will be introduced, along with an overview of promising applications enabled by these phenomena.

Delocalization

A hallmark feature of polaritons is their delocalized nature inherited from their photonic part. Unlike conventional excitons in organic materials, which are typically localized on individual molecules and migrate through short-range, incoherent mechanisms such as Förster or Dexter transfer, polaritons emerge as spatially extended, coherent states.

Under strong coupling regime, polaritons, hybrid light–matter states, are collectively shared among a large number of molecules. As a result, the polaritonic wavefunction is not confined to a single molecule, but instead spans distances comparable to, or exceeding, the optical wavelength. This spatial extension enables nonlocal interactions, allowing energy transfer and exciton migration to occur efficiently over micrometer scales, well beyond the nanometric limits of conventional excitonic transport.

This delocalization is particularly important in disordered molecular systems, where traditional exciton hopping is inefficient and random. By contrast, polaritonic states enable enhanced energy transport and long-range molecular interactions,

offering a powerful strategy for manipulating optoelectronic properties and facilitating new functionalities in organic materials. Over the past decade, these collective light–matter interactions have attracted significant interest as a platform for tailoring material behavior and energy dynamics beyond the limits of localized excitonic models [7–10].

Mode selectivity and tunability

The Fabry–Pérot microcavity is one of the most commonly employed architectures for realizing strong light–matter coupling. Its structural simplicity allows for the efficient integration of polaritonic states into functional optoelectronic devices. Since polaritons are formed within optical microcavities, they naturally inherit key cavity properties such as spectral tunability and mode selectivity. These features have recently utilized in the development of narrowband polariton OLEDs [11–13] and spectrally tunable polariton OPDs [14, 15]. Beyond these optical characteristics, the hybrid light–matter nature of polaritons enables interaction with the molecular excitonic component, paving the way for the modulation of photophysical processes at the molecular level [16]. For instance, recent studies have demonstrated that introducing strong coupling in TADF molecules can modify the rate of RISC. This was achieved by coupling the singlet excited state (S_1) to the cavity mode, effectively shifting the lower polariton (LP) energy and thereby reducing the energy gap between S_1 and T_1, which enhances the RISC rate [17, 18].

Effective mass control

An intriguing consequence of the hybrid light–matter nature of polaritons is their effective mass, which differs significantly from that of either pure excitons or photons. Rather than being fixed, the polariton effective mass can be tuned by adjusting the Hopfield coefficients, which determine the relative photonic and excitonic character of the polaritonic state. This tunability allows for tailoring polariton properties to suit specific applications. For example, in the context of Bose–Einstein condensation (BEC), where a low effective mass is essential for achieving quantum degeneracy at elevated temperatures, polaritons are engineered to be more photonic in nature [19]. In contrast, for optoelectronic devices such as OLEDs and OPDs, where low angular dispersion and direction-independent operation are critical, polaritons are designed to be more excitonic. This results in an exciton-like dispersion that suppresses angular sensitivity, making them more suitable for practical device integration [11].

Despite nearly a decade of research and development in polariton-based devices, their performance still lags behind that of state-of-the-art optoelectronic technologies. This highlights a significant gap in the field of polaritronics, the emerging discipline at the intersection of polariton physics and electronic device engineering, underscoring the need for further innovation to bridge the divide between fundamental polariton science and practical applications. Bridging this divide is the core objective of this thesis, which aims to explore strategies for translating fundamental polaritonic effects into practical, high-performance organic optoelectronic devices.

---

2 Origin of Delayed Electroluminescence in a Polaritonic OLED

This chapter has been adapted from: Ahmed Gaber Abdelmagid, Hassan A. Qureshi, Michael A. Papachatzakis, Olli Siltanen, Manish Kumar, Ajith Ashokan, Seyhan Salman, Kimmo Luoma, and Konstantinos S. Daskalakis. "Identifying the origin of delayed electroluminescence in a polariton organic light-emitting diode". Nanophotonics, 2024; 14: 2565-2573.

2.1 Motivation

One of the most intuitive applications of polaritons is to exploit the new eigenstates they introduce in molecular systems, thereby modulating processes whose rates depend on energy-level separations. By engineering these light–matter hybrid states, polariton chemistry reshapes molecular energy landscapes and enables room-temperature control of photophysical and photochemical dynamics [4, 20–22]. A representative example is RISC in OLEDs, where triplet excitons are upconverted to singlet excitons (Device Note #5). Analogous to molecular design strategies, adjusting microcavity parameters can tune the LP mode into resonance with triplet energies, potentially assisting, or even facilitating, triplet-to-singlet population transfer. Motivated by these prospects, researchers have explored polaritonic strategies to modulate RISC rates. Under optical excitation, several studies have probed how strong coupling influences RISC in TADF emitters [17, 18, 23, 24]. A central, ongoing debate concerns the collective nature of strong coupling in organic films: because the photonic component of polariton modes is highly delocalized over many molecules, any polaritonic impact on intramolecular nonradiative pathways can be diluted at the single-molecule level [25]. Although TADF systems offer a convenient testbed, their intrinsically fast RISC can mask subtler polariton-induced rate changes, making them difficult to resolve experimentally. To deepen insight, it is therefore advantageous to extend these studies to conventional fluorescent emitters. Moreover, unlike previous studies, in this chapter, the dynamics are measured under electrical excitation in an operational OLED. Electrical injection populates excitons according to spin statistics—25% singlets and 75% triplets, thereby directly generating a substantial triplet population in a device that employs a fluorescent emitting layer.

2.2 Device design

The device architecture employs a well-established fluorescent emitter for organic polaritonics, specifically, TDAF, that has been extensively studied [19, 26, 27]. This material was chosen because (i) its singlet–triplet splitting ΔE_{S-T} is $\sim$ 0.8 eV, rendering RISC negligible [28]; (ii) it exhibits a large oscillator strength, enabling substantial Rabi splitting and thus permitting polaritonic hybridization to reduce the effective ΔE_{S-T}; and (iii) TDAF's ambipolar charge transport makes it particularly well suited for polaritonic OLED studies as it allows uniform microcavity and keep the architecture simple [27]. This also enabled device architecture in its simplest form, where the emitting layer (TDAF) is directly sandwiched between the hole injection layer and the electron injection layer. **Figure 16a** shows a Jablonski-style diagram of a strongly coupled organic emitter under electrical excitation, highlighting potential polariton-assisted RISC pathway between singlet and triplet manifolds, and **Figure16b** the corresponding microcavity OLED stack used in this work.

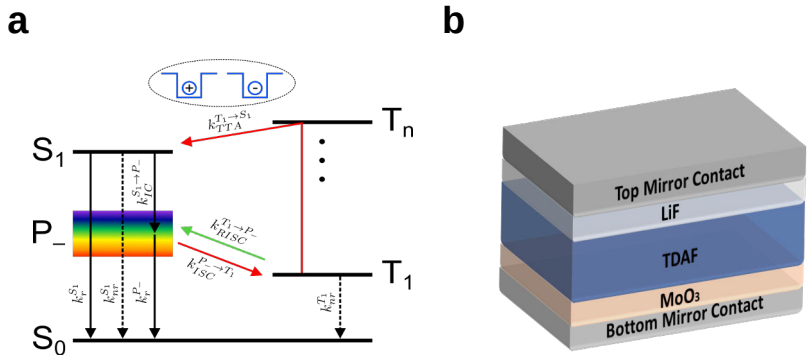

Figure 16. (a) Energy-level schematic of the coupled light–matter system showing singlet states (S_0, S_1), the lower polariton (LP), and the triplet manifold (T_1, T_n). Arrows indicate intersystem crossing (ISC), reverse intersystem crossing (RISC), triplet–triplet annihilation (TTA), and radiative/nonradiative decay channels under electrical excitation. (b) Cross-sectional architecture of the polaritonic OLED: bottom mirror contact/MoO_3/TDAF/LiF/top mirror contact.

2.3 Polariton formation

Three polaritonic OLEDs were fabricated to progressively shift LP toward the triplet manifold, yielding normal-incidence LP energies of 2.95, 2.83, and 2.67 eV. **Figure 17a–c** presents false-color, angle-resolved reflectivity maps for the three devices. From coupled-oscillator fits, the vacuum Rabi splittings are 0.92, 0.88, and 0.96 eV for devices (a)–(c), respectively. The magnitude ($\sim$ 0.9 eV) places the system in the ultrastrong-coupling regime for a 3.55 eV exciton, shifting the LP well below the bare exciton and allowing detuning toward the triplet manifold to control RISC.

Another advantage of the large Rabi splitting is that the lower polariton retains a high excitonic fraction even under strong negative detuning. Maintaining substantial exciton content is crucial for polaritons to couple to other molecular states at the intramolecular level [18]. The excitonic and photonic content are presented in **Publication I**.

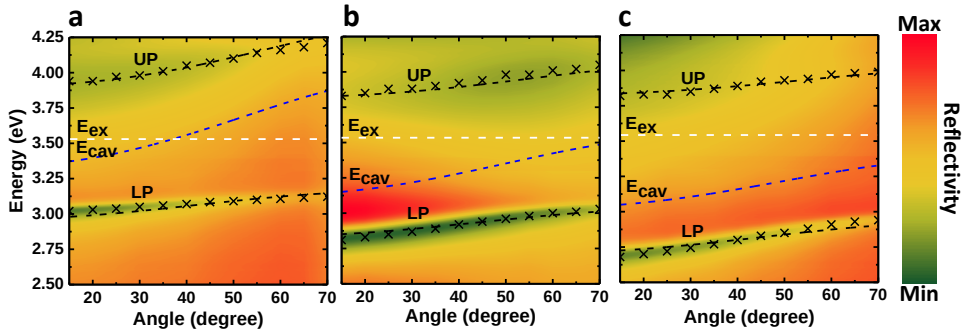

Figure 17. Angle-resolved reflectivity for three microcavity OLEDs with varying detuning. Dark dispersive features correspond to the LP and UP branches. The dashed blue line marks the bare cavity mode E_{cav}, and the dashed white line indicates the exciton energy E_{ex}. Dashed lines denote the coupled-oscillator fits. From (a) to (c), increased negative detuning lowers the LP energy (2.95, 2.83, and 2.67 eV at normal incidence), pushing the LP closer to the triplet manifold.

2.4 Time-Resolved Electroluminescence

To probe triplet–to–singlet dynamics, attention is directed to the delayed emission associated with RISC, which occurs on microsecond–millisecond (μs–ms) timescales. Under optical excitation, time-resolved photoluminescence is typically employed; in an OLED configuration, the appropriate technique is time-resolved electroluminescence (TREL). Experimental details are provided in the Supplementary Information of **Publication I**. Samples are driven with square voltage pulses featuring sub-9 ns rise and fall times, and emission is recorded using a time-correlated single-photon counting (TCSPC) setup. To ensure measurement consistency, the pulse duration and repetition rate are chosen so that the device reaches steady state before the electrical pulse is switched off, after which the emission decay is acquired.

TREL was first measured on a reference device with an otherwise identical stack but employing ITO as the bottom electrode (**Figure 18**). **Figure 18a** illustrates the device architecture (glass/ITO/MoO_3/TDAF/Al/LiF). **Figure 18b** shows the semi-logarithmic electroluminescence decay (gray) recorded after bias turn-off, alongside a rate-equation decomposition into TADF (green), triplet–triplet annihilation (TTA, red), and trap emission (TE, blue). The fitted model indicates that trap-state emission dominates the decay. Full details of the model are provided in Section 2.3 of **Publication I**.

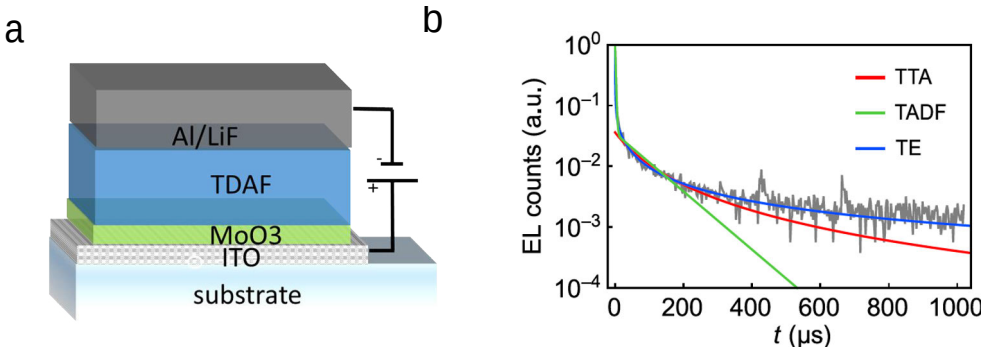

Figure 18. Reference OLED for TREL measurements and decay analysis. (a) Schematic cross-section of the device: glass/ITO anode, MoO_3 hole-injection layer, TDAF emitting layer, and Al/LiF cathode. (b) Semi-log time-resolved electroluminescence following bias turn-off (gray), together with a rate-equation fit into thermally activated delayed fluorescence (TADF, green), triplet–triplet annihilation (TTA, red), and trap emission (TE, blue).

2.4.1 TREL of Polaritonic OLEDs

TREL was measured for the three polaritonic OLEDs. Few scenarios are anticipated as the LP is tuned relative to the triplet manifold ($\Delta E_{\mathrm{LP}-T}$ denotes the LP–triplet energy offset): (i) a TADF-like channel opens, enabling population transfer from molecular triplets to the LP and thereby modifying the delayed-emission lifetime [17, 18]; (ii) a direct transition from molecular trap states to the LP becomes active, likewise altering the delayed component [29]; or (iii) no additional pathways arise and the decay remains governed by trap emission (TE), as in the reference device [23, 25]. **Figure 19** compiles the TREL of the polaritonic OLEDs. At an injection current of $J \approx 90\ \mathrm{mA\,cm^{-2}}$ (**Figure19a**), the decays of POLED 1–3, despite progressively bringing the LP closer to T_1, are essentially indistinguishable, indicating that any polariton–triplet alignment effect on the delayed emission of TDAF is negligible in the raw data. Consistent behavior is observed when sweeping the drive current from $\sim$ 30 to $\sim$ 150 $\mathrm{mA\,cm^{-2}}$ (**Figure19b**), with only minor changes in the long-time slope and a slight current-dependent quenching at higher currents. To identify the origin of the delayed component and this quenching, a rate-equation model was used to fit the measured traces; the fits are consistent with TE-dominated delayed EL, supporting scenario (iii). *All measurements were performed at a constant current density, which directly sets the excitation density, because the system's kinetics and spectra are highly sensitive to excitation density.*

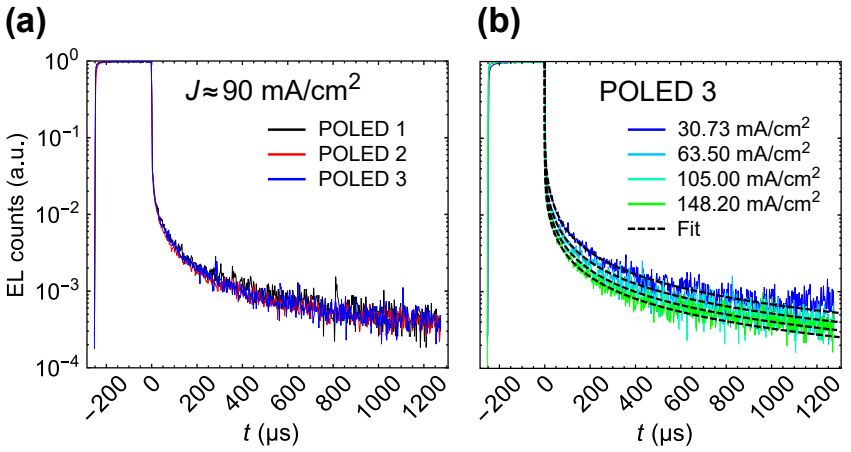

Figure 19. TREL after bias turn-off. (a) Decay traces for POLED 1–3 at an injection current of $J \approx 90\ \mathrm{mA\,cm^{-2}}$ show nearly identical delayed-emission profiles despite different detunings. (b) POLED 3 measured at 30.73, 63.50, 105.00, and 148.20 $\mathrm{mA\,cm^{-2}}$; dashed curves are rate-equation fits. The long-time tail is only weakly current dependent, with slight quenching at higher drive.

2.5 Conclusions

TREL was used to probe polaritonic OLEDs alongside a non-cavity reference. Despite tuning the LP across the TDAF energy landscape, including conditions where the LP approaches the T_1 level, the delayed EL dynamics remain essentially unchanged across devices and over a current range of $\sim$ 30–150 $\mathrm{mA\,cm^{-2}}$. Coupled rate-equation analysis attributes the delayed component primarily to trap-assisted emission, with no resolvable signatures of a TADF-like triplet$\rightarrow$LP pathway or a direct trap$\rightarrow$LP transition. The large Rabi splittings (~ 0.9 eV) confirm robust strong coupling, yet any polariton–triplet alignment effect on TDAF delayed emission appears negligible within the sensitivity of these measurements.

A likely explanation is the collective, highly delocalized nature of polaritons: because a polariton is shared by N molecules, its overlap with any single-molecule state (e.g., a triplet or a trap) scales as $1/N$, rendering direct interaction negligibly small [16, 23, 25].

Building on this conclusion, that polaritonic effects on intramolecular processes are negligible in the present system, the following chapters pivot from microscopic tuning to macroscopic device-engineering strategies, with the aim of realizing organic polariton optoelectronic architectures whose performance rivals state-of-the-art technologies.

2.6 Author contributions

K.S.D. conceived and guided the project. **A.G.A.** fabricated the samples. O.S. developed the theoretical model. O.S. and **A.G.A.** analysed the experimental data. **A.G.A.**, H.A.Q., and M.A.P. developed and performed the measurements. A.A. and S.S. performed the quantum chemical calculations. **A.G.A.**, O.S., and K.S.D. wrote the manuscript.

3 Polaritonic Design for Narrowband, Angle-Independent NIR OPD

This chapter has been adapted from: Ahmed Gaber Abdelmagid, Zhuoran Qiao, Boudewijn Coenegracht, Gaon Yu, Hassan A. Qureshi, Thomas D. Anthopoulos, Nicola Gasparini, and Konstantinos S. Daskalakis. "Polaritons in non-fullerene acceptors for high responsivity angle-independent organic narrowband infrared photodiodes". Advanced Optical Materials, 2025; e01727

3.1 Motivation

Wavelength-selective photodetectors are essential for spectroscopic sensing, including applications such as biomedical sensing, chemical composition analysis, and ingredient identification. OPDs enable device miniaturization thanks to their flexibility, low cost, and ease of fabrication. However, achieving narrowband absorption in organic semiconductors remains challenging (Device Note #3) [30–33]. To address this, several strategies have been explored. Self-filtering designs can deliver narrow spectral response, but they typically require μm-thick active layers with tightly specified optical and electrical properties, which restricts material choices [34–37]. Optical microcavities offer spectral selectivity and tunability; however, they exhibit pronounced angular dispersion, often shifting the absorption peak by up to ~ 50 nm at 45° incidence (Device Note #8), thereby limiting applications that demand a wide field of view [38–45]. Moreover, the performance of cavity-based OPDs is limited because it relies on amplifying the weak CT absorption, which is orders of magnitude smaller than the intrinsic absorption.

Because polaritons are naturally formed in optical cavities, they can retain the advantages of cavity-based OPDs while mitigating core limitations by offering intrinsic mode selectivity and reduced angular dispersion, as discussed in Section 1.3.3. Polaritons have been employed to realize NIR OPDs [14, 15]; however, their performance still lags behind the state-of-the-art. In this chapter, an OPD tailored for NIR applications is designed and engineered, deliberately leveraging macroscopic device strategies, rather than intramolecular polaritonic effects, to achieve high responsivity and narrowband spectral selectivity.

3.2 Device design

To overcome the limitations of cavity-based CT OPDs, the device concept builds on a highly efficient broadband OPD platform. This approach relies on two key attributes: (i) active materials with a high absorption coefficient, and thus large oscillator strength, providing control over the excitonic fraction in the polariton branches and, in turn, helping to reduce angular dispersion; (**Figure 20a**) and (ii) an optimized diode architecture with appropriate transport and blocking layers, yielding high responsivity (**Figure 20b**). The active medium of the polariton OPDs is a PTB7-Th:IEICO-4F blend. IEICO-4F is selected for its large oscillator strength and its favorable film morphology when blended with PTB7-Th, both critical for achieving strong coupling in planar microcavities [20, 46, 47]. Moreover, IEICO-4F has underpinned high-performance broadband OPDs thanks to its high charge mobility, efficient charge transport, and chemical/thermal stability [48–51]. The devices fabricated in this chapter use the stack: ITO | Ag (25 nm) | MoO_x (10 nm) | PTB7-Th:IEICO-4F (x nm) | C_{60}:LiF (25 nm) | Ag (100 nm). The reference broadband device employs the same layer sequence but without the semitransparent Ag. It exhibits a broadband photoresponse with spectral responsivity exceeding $0.40\ \mathrm{A\,W^{-1}}$ in the 760–860 nm range. Beyond 900 nm, the responsivity declines, consistent with the reduced absorption of IEICO-4F (**Figure 20c**).

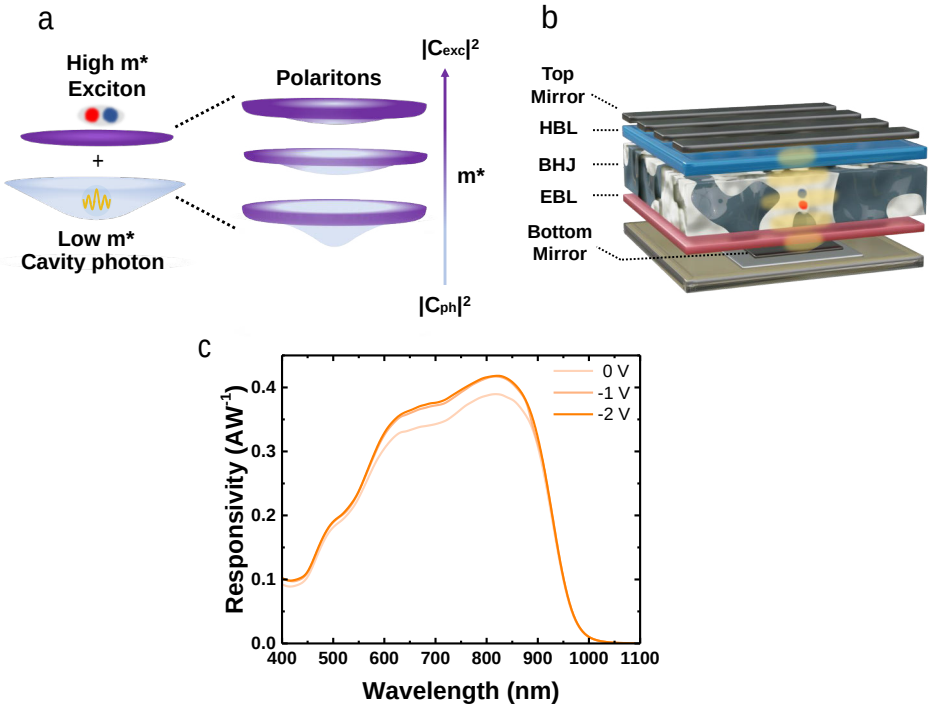

Figure 20. (a) Schematic of polariton formation in a planar microcavity: a heavy-mass exciton couples to a light-mass cavity photon to yield polariton modes whose composition (Hopfield coefficients $|C_{\mathrm{exc}}|^2$, $|C_{\mathrm{ph}}|^2$) and effective mass m^*, higher m^* leads to more excitonic character and thus, exciton-like dispersion. (b) Polaritonic OPD architecture employing a microcavity with bottom and top mirrors, an electron-blocking layer (EBL), a bulk-heterojunction (BHJ) active layer, and a hole-blocking layer (HBL). (c) Responsivity spectra of the reference device at different bias voltages.

3.3 Polariton formation

Figure 21 shows false-color, angle-resolved reflectivity maps for two polaritonic OPD designs with active layer thicknesses 92 nm and 99 nm for devices A and B, respectively (a, b). Clear anticrossings at wavelengths corresponding to the PTB7-Th ($\sim$ 710 nm) and IEICO-4F ($\sim$ 835 nm) excitons yield three polariton branches, UP, MP, and LP, confirming effective coupling between the cavity photon and both molecular excitons. The red dashed lines are coupled-harmonic-oscillator (CHO) fits: from these, panel (a) gives two vacuum Rabi splittings of 0.57 eV and 0.31 eV with a detuning $\Delta = E_{\mathrm{c}} - E_{\mathrm{IEICO\text{-}4F}} = 0.41$ eV; panel (b) yields splittings of 0.55 eV and 0.32 eV with $\Delta = E_{\mathrm{c}} - E_{\mathrm{IEICO\text{-}4F}} = 0.33$ eV. The chosen detunings keep the LP in the NIR. Hopfield analysis of the LP shows a substantial IEICO-4F excitonic contribution of $\approx 60\%$ and $\approx 50\%$ for devices A and B, respectively. This high exciton content increases the LP's effective mass and imparts an exciton-like

optical response. Angle-resolved reflectivity map for one more detuning, device C, is presented in the supplementary information of **Publication II**.

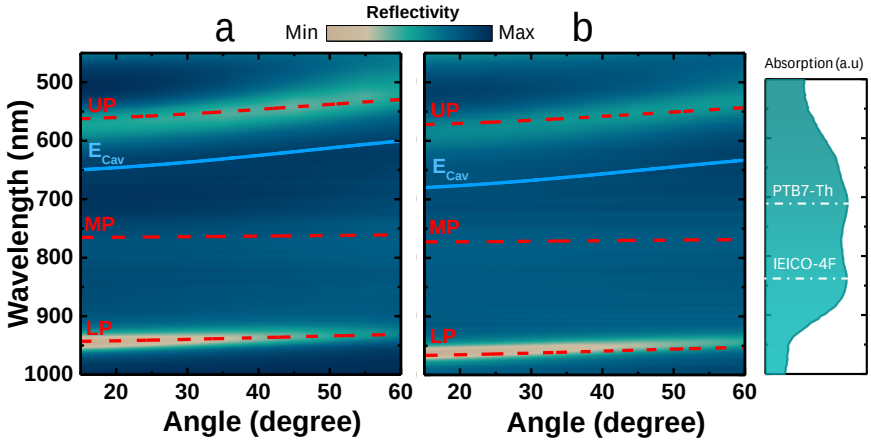

Figure 21. Angle-resolved reflectivity of polaritonic OPD microcavities. (a,b) False-color reflectivity maps versus detection angle; dark bands indicate reflectivity minima. The light-blue line traces the bare cavity dispersion E_{cav}. The red dashed lines are CHO fits to UP, MP, and LP branches. The main absorption features of the blend (right panel).

3.4 Electrical performance

To evaluate the polaritonic OPD performance, this section presents the electrical and optoelectronic characterization of device A, including current–voltage behavior under dark and illumination, spectral responsivity, and dynamic response (rise/fall times and -3 dB bandwidth). **Figure 22a** shows the current–voltage characteristics of the device A (LP resonance at 965 nm) under dark and illuminated conditions. A dark current density of 9.29×10^{-7} A cm^{-2} at -2 V is recorded, the photocurrent density reaches $J_{\mathrm{L}} = 1.04 \times 10^{-3}$ A cm^{-2} at -2 V. **Figure 22b** presents the responsivity spectrum at -2 V. The device attains a peak responsivity of 0.23 A W^{-1} at 965 nm and 0 V, which increases slightly to 0.24 A W^{-1} at -2 V, typical operating conditions for OPDs [52]. Dynamic performance was assessed at -2 V. Under NIR illumination, the device shows a rise time of 1.6 μs and a fall time of 1.1 μs (**Figure 22c**). The -3 dB cut-off frequency reaches 412 kHz under 970 nm modulation (**Figure 22d**), highlighting the suitability of the polaritonic OPD for fast imaging applications [30, 53]. Within experimental resolution, polaritons did not measurably alter the microscopic steady-state or transient characteristics (**Supplementary Figure S11 in Publication II**)

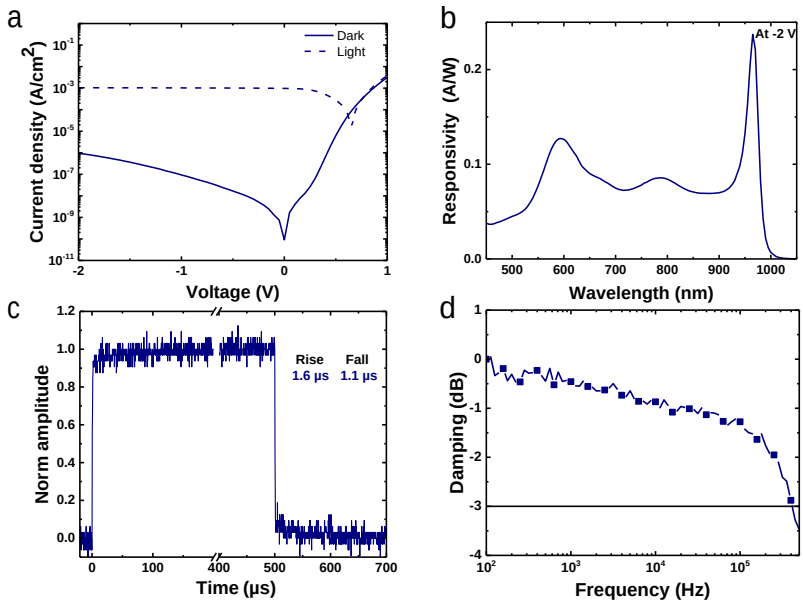

Figure 22. a) Dark and light J-V curve of the optimized device, polaritonic OPD with resonance wavelength at 965 nm. b) Responsivity at –2 V. c) Transient photoresponse of the polariton OPD at –2 V under 970 nm NIR light. d) Cut-off frequency of the polariton OPD at –3 dB at –2 V under 970 nm NIR light

3.4.1 Responsivity enhancement

By virtue of their photonic fraction, inherited from the cavity photon, polaritons can act as cavity resonances, selectively enhancing resonant transitions while suppressing off-resonant absorption, thereby yielding spectral narrowing and increased quantum efficiency. In a Fabry–Pérot–type cavity, FWHM of the resonance scales with the active-layer absorption coefficient α (FWHM $= \alpha\lambda^2/n\pi$); increasing α broadens the passband, while reducing α yields a sharper (narrower) resonance. At the same time, the peak EQE rises with α because a larger fraction of the intracavity field is absorbed in the active layer rather than lost in the mirrors (EQE $= \alpha/(\alpha + 2r/L)$, where n is the refractive index, λ the resonance wavelength, r the effective mirror loss, and L the cavity length) [40]. The device designer therefore balances a fundamental trade-off: narrow bandwidth (small α) versus high EQE (large α).

In the polaritonic OPDs, the LP is deliberately tuned into the above-gap, low-absorption region of the PTB7-Th:IEICO-4F blend, a regime of modest material absorption that is nevertheless far stronger than the CT absorption exploited in earlier cavity-based OPDs. This yields a higher EQE (responsivity) according to (EQE $= \alpha/(\alpha + 2r/L)$. Operating at a small effective absorption coefficient α places the devices on the "narrowband" side of the trade-off, yielding sharp peaks (**Figure 23a**). By contrast, shifting the resonance to shorter wavelengths (~ 920 nm), where α is larger, leads to a

markedly broader bandwidth (FWHM > 100 nm) and a reduced responsivity relative to the reference device (**Supplementary Figure S7 in Publication II**).

Devices exhibit a sharp LP resonance superimposed on a weak material background, and the enhancement over the reference increases as the LP is detuned to longer wavelengths, where the blend's intrinsic absorption is lower and the LP's excitonic fraction is higher (**Fig. 23b**). In short, by positioning the LP on the low-absorption tail, the cavity–polaritonic selectivity delivers a directed narrowband response while preserving useful responsivity by selectively amplifying that tail.

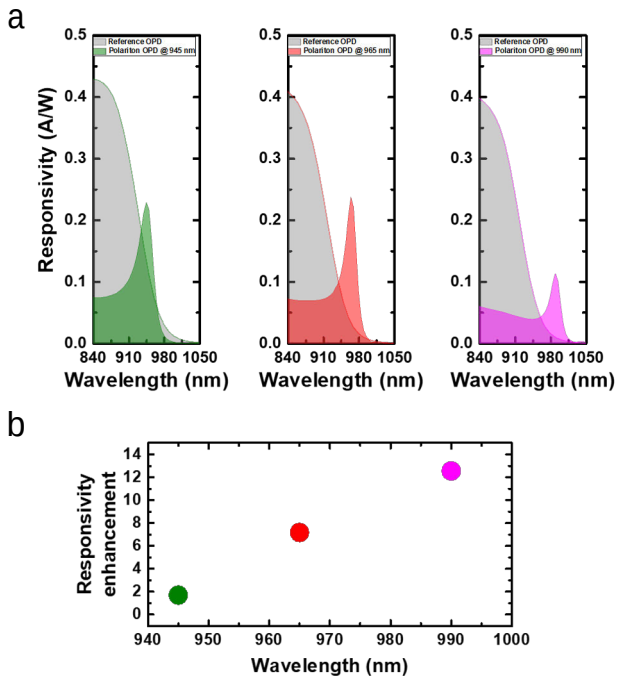

Figure 23. NIR responsivity of polaritonic OPDs relative to a broadband reference. (a) Responsivity spectra for three devices with the LP tuned to ~ 945, ~ 965, and ~ 996 nm (green, red, magenta). The gray trace shows the broadband reference OPD (identical stack without the semitransparent Ag). (b) Responsivity enhancement, defined as the ratio of the polaritonic OPD peak to the reference at the same wavelength, plotted versus LP wavelength. The enhancement increases as the LP is shifted deeper into the low-absorption tail and as the LP photonic fraction grows.

3.5 Angular spectral stability

Angle-resolved responsivity measurements were performed to quantify the angular dispersion of the polaritonic OPDs (**Figure 24a**). In contrast to previously reported cavity-based OPDs [38–45], the polaritonic devices show markedly reduced disper-

sion: the responsivity peak shifts by only ~ 9 nm in the thinnest devices and by at most ~ 16 nm in the thickest. This reduced angular dependence highlights the benefits of strong coupling and correlates directly with the excitonic fraction of the LP, as shown in **Figure 24b** for devices A, B, and C. At normal incidence, all devices exhibit a responsivity peak with FWHM < 45 nm (**Figure 24c**). The bandwidth narrows as the resonance is tuned into regions of smaller absorption coefficient α, consistent with the cavity relation $\mathrm{FWHM} = \alpha\lambda^2/(n\pi)$. To relate bandwidth to angular dispersion, **Figure 24d** plots the angle-invariance factor, defined as angular dispersion divided by the FWHM, versus wavelength, showing that the devices operate, in practice, in an angle-independent regime.

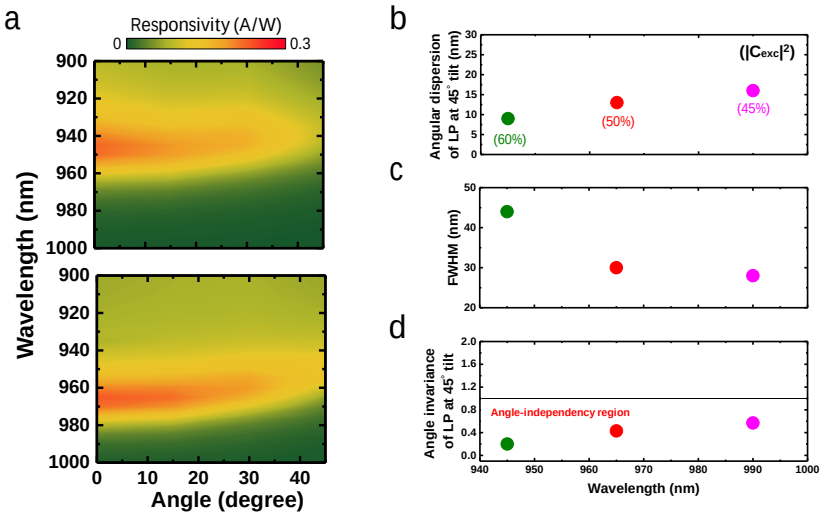

Figure 24. Angle-resolved responsivity of polaritonic OPDs. (a) False-color maps from $0°$ to $45°$ in $15°$ steps for device A (top) and device B (bottom). (b) LP angular dispersion (peak shift at $45°$, in nm) for devices A–C; values in parentheses indicate the LP excitonic fraction ($|C_{\mathrm{exc}}|^2$). (c) Full width at half maximum (FWHM) of the LP peak. (d) Angle-invariance metric of the LP (see text). Color coding: device A (olive), device B (red), device C (magenta).

3.6 State-of-the-art

Figure 25 benchmarks our narrowband NIR polaritonic OPDs against representative reports spanning 945–990 nm. Our devices deliver $0.23\ \mathrm{A\,W^{-1}}$ at 945 and 965 nm, and $0.11\ \mathrm{A\,W^{-1}}$ at 990 nm, while maintaining thin active layers ($\sim$ 92–110 nm). The accompanying table summarizes data at 0 V bias: comparable or higher responsivities in prior work often rely on substantially thicker photoactive layers (hundreds of nanometers up to $\sim 2\ \mu\mathrm{m}$); for example, $0.24\ \mathrm{A\,W^{-1}}$ at 940 nm with a 2 μm layer, and $0.14\ \mathrm{A\,W^{-1}}$ at 980 nm with a 500 nm layer (**Table 1**). Collectively, these metrics place the devices among the state-of-the-art for narrowband NIR OPDs. Their

performance is competitive with leading reports, yet achieved with a stack an order of magnitude thinner. This underscores the promise of the polaritonic approach for compact, high-performance NIR detection suited to miniaturized spectroscopy.

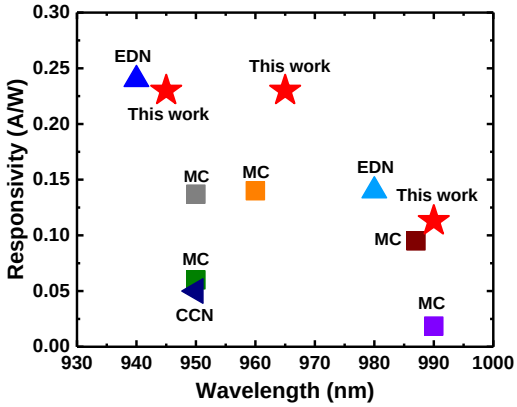

Figure 25. Comparison of the responsivities of narrowband OPDs at 0 Vwith peak wavelengths between 940 and 990 nm

Wavelength (nm)	Responsivity (A/W)	Active layer thickness (nm)	Reference
940	0.24	2000	12
945	**0.23**	**92**	**This work**
950	0.06	1500	10
950	0.05	220*	19
950	0.137	50#	15
960	0.14	440	16
965	**0.23**	**99**	**This work**
980	0.14	500	13
987	0.095	∼180	18
990	**0.11**	**110**	**This work**
990	0.0185	-	20

Table 1. Overview of reported narrowband NIR-OPDs to date with peak wavelength ranging from 940 to 990 nm at 0 V

3.7 Conclusions

This chapter established a polaritonic design approach to narrowband NIR OPDs that utilizes macroscopic cavity effects. A central outcome is the experimentally verified link between the lower polariton's excitonic fraction and the device's angular stability. When the LP is tuned into the above-gap, low-absorption region of the PTB7-Th:IEICO-4F blend, Hopfield analysis indicates a substantial excitonic fraction. Increasing this fraction raises the LP's effective mass and drives its character toward a flat, exciton-like dispersion, thereby suppressing the strong angle dependence inherited from the light, highly dispersive cavity photon. Consistently, the polaritonic OPDs exhibit minimal angular dispersion, responsivity-peak shifts of only ~ 9–16 nm up to 45°, together with narrow spectral features (FWHM < 45 nm) and a low angle-invariance factor across the operating band.

Beyond the angle-stable narrowband response, the architecture delivers responsivity competitive with the state of the art, $0.23\ \mathrm{A\,W^{-1}}$ at 945 and 965 nm and $0.11\ \mathrm{A\,W^{-1}}$ at 990 nm at $0\ \mathrm{V}$, while employing substantially thinner active layers than many prior reports. This performance arises from operating in a regime of modest material absorption (α) within the PTB7-Th:IEICO-4F blend, rather than relying on the much weaker CT absorption used in earlier cavity-based OPDs.

These results show that deliberately engineering a high LP excitonic fraction, through material choice, detuning, and cavity design, provides a practical lever for angle-independent, narrowband NIR detection without sacrificing responsivity. With straightforward refinements (optimized blocking layers, mirror reflectivity, and detuning to balance selectivity and efficiency), the polaritonic architecture offers a compact, manufacturable platform for miniaturized spectroscopy and fast imaging.

3.8 Author contributions

A.G.A., T.D.A., and K.S.D. initiated the project. **A.G.A.** designed the project, fabricated the devices, performed the majority of experiments, and analyzed the data. Z.Q. together with **A.G.A.** performed the optoelectronic measurements, supervised by N.G.. H.A.Q. performed the high-resolution reflectivity measurements. B.C. and G.Y. contributed to the sample fabrication and characterization. **A.G.A.** and K.S.D. wrote the manuscript. K.S.D. supervised the project. All authors contributed to the draft, discussion, and analysis of the data.

4 Polaritonic Engineering for Record-Performance NIR OLEDs

The work presented in this chapter was carried out at the Humboldt Centre for Nano- and Biophotonics, Institute for Light and Materials, University of Cologne, Germany, as part of an international research internship.

The manuscript: Ahmed Gaber Abdelmagid, Andreas Mischok, Malte C. Gather, and Konstantinos S. Daskalakis "Polaritonic Engineering for Record-Performance Near-Infrared OLEDs". Under preparation, 2025

4.1 Motivation

OLEDs are the cornerstone of modern display technology and are increasingly explored for NIR applications, including biomedicine, optical communication, and security [54–56]. State-of-the-art NIR OLEDs employ either phosphorescent heavy-metal complexes or purely organic emitters such as TADF molecules [55, 57]. While the former deliver high internal quantum efficiencies, their reliance on scarce heavy elements raises sustainability concerns. Purely organic TADF emitters are environmentally benign and, in principle, enable 100% exciton harvesting via RISC through a donor–acceptor (D–A) design that minimizes HOMO–LUMO overlap and reduces the ΔE_{ST}.

However, TADF molecules typically exhibit broad emission bandwidths (Device Notes #2 and #3) and, when pushed into the NIR, suffer from enhanced non-radiative decay rates governed by the energy-gap law (Device Note #6) [54–57]. As a result, TADF-based NIR OLEDs are often broadband (>100 nm) with a significant portion of their emission spectrum in the visible region (<700 nm), and their EQE drops markedly when the peak wavelength is pushed deep into the infrared (>750 nm), as shown in **Figure 26** [57].

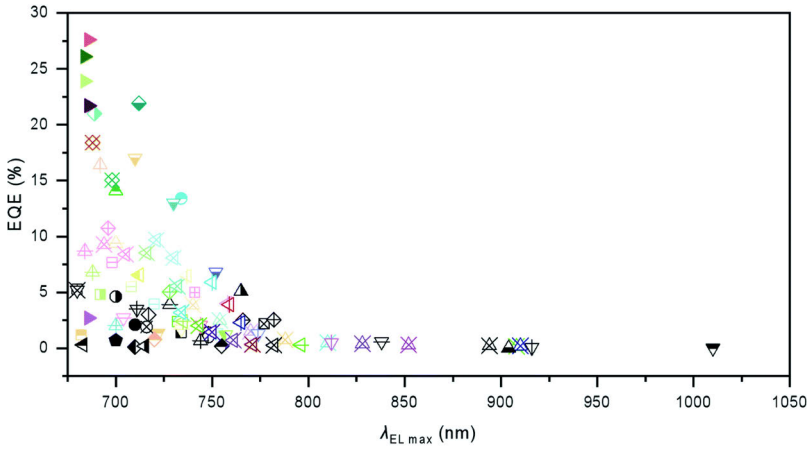

Figure 26. EQE of representative NIR TADF OLEDs [57].

As discussed in Section 1.3.3, exciton–photon polaritons offer a unique route to reshape emission properties. By engineering the photonic environment, polaritons can narrow spectra and enhance outcoupling. Inspired by the successful development of efficient polaritonic NIR OPDs presented in the previous chapter, this chapter introduces a novel polariton-based OLED design. This approach achieves record-high efficiencies in the NIR while addressing the intrinsic limitations of TADF emitters in this spectral range.

4.2 Device design

The design concept is based on an intracavity pumping structure [11], in which a highly efficient deep-red/NIR OLED, featuring a peak wavelength around 700 nm and a broad emission spectrum extending beyond 800 nm, is used as the EML. A strong coupling layer (SCL) incorporating an NIR-absorbing dye is then introduced to enable polariton formation. In this configuration, the LP mode is radiatively pumped by photons from the red tail of the EML emission. DCN-SPTPA was selected as the EML material, as it has been shown to yield highly efficient OLEDs [58]. **Figure 27** presents the emission spectrum of 20 wt% DCN-SPTPA doped in CBP, exhibiting deep-red/NIR emission with a peak at 705 nm and a broad linewidth of approximately 130 nm. For the SCL, SubNC, commonly used as an active material in organic photovoltaics due to its high extinction coefficient, was chosen. Moreover, SubNC has been demonstrated to form polaritons in thin films [59], and its absorption spectrum overlaps well with the emission of DCN-SPTPA (**Figure-27**).

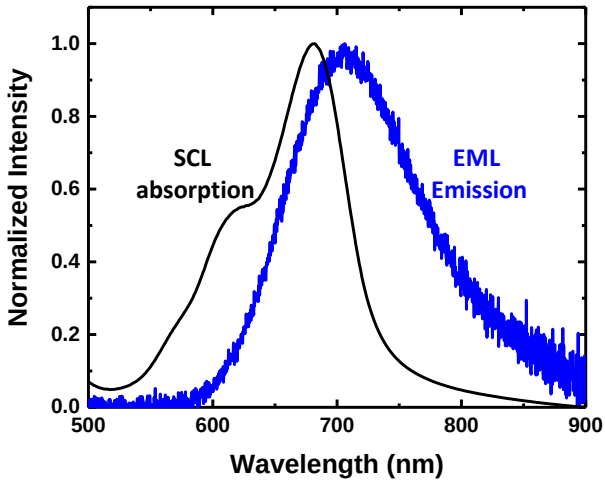

Figure 27. Normalized emission spectrum of the emissive layer (EML, 20 wt% DCN-SPTPA in CBP, blue) and absorption spectrum of the strong coupling layer (SCL, SubNC, black).

With the key components of the device design—the EML and SCL—fixed, the device was fabricated following the literature-reported architecture [58], with targeted modifications to support polariton formation. Specifically, the structure employs two metal electrodes: a thick reflective electrode and a semi-transparent top electrode to define the optical cavity. The SCL is realized by incorporating SubNC into the HTL, while F6TCNNQ is used as a p-type dopant to maintain high conductivity as the cavity is detuned to the desired wavelength by changing the thickness of the SCL layer. **Figure 28** illustrates the resulting device architecture: Ag | MoO_x | x nm TAPC:SubNC:F6TCNNQ | 10 nm TAPC | 10 nm TCTA | 10 nm mCP | 20 nm CBP:20 wt% DCN-SPTPA | 55 nm TmPyPB | 1 nm LiF | 100 nm Al.

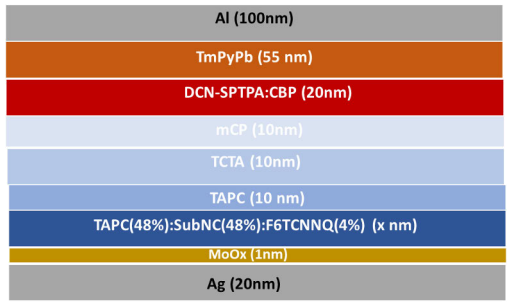

Figure 28. Schematic of the polaritonic NIR OLED architecture.

4.3 Polariton formation

To confirm polariton formation, angle-resolved reflectivity measurements were performed on a device engineered to push the LP mode beyond 750 nm. This was achieved by selecting an SCL thickness of 60 nm for Device A, thereby setting the cavity detuning and shifting the LP dispersion deeper into the NIR. The angle-resolved reflectivity spectra exhibit three clear dispersive minima corresponding to UP, MP, and LP branches. At low angles, the LP is positioned at ∼780 nm for Device A, consistent with the design target.

Figure 29 presents the false-color angle-resolved reflectivity map for Device A with coupled-oscillator fits overlaid (blue curves). Pronounced avoided crossings yield three branches, evidencing strong light–matter coupling. Fitting the dispersion gives Rabi splittings of $\hbar\Omega_{0-0} = 0.22$ eV and $\hbar\Omega_{0-1} = 0.348$ eV (220 and 348 meV), confirming effective polariton formation with the LP branch residing in the near-infrared.

It is important to note that the DCN-SPTPA absorption band at 518 nm is dominated by CT character and therefore exhibits low oscillator strength (Device Note #2). Accordingly, strong coupling to the EML transition is not expected; the observed polaritonic splitting originates from coupling of the cavity photon to the SubNC excitons within the SCL.

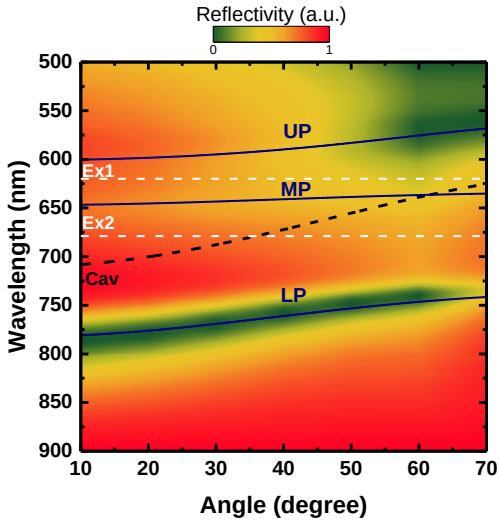

Figure 29. Polariton characteristics of the polariton OLED. Angle-resolved reflectivity map for Device A. The dashed black curve traces the bare cavity dispersion (Cav), while the horizontal white dashed lines (Ex1 and Ex2) mark the SubNC 0–0 and 0–1 excitonic resonances. The blue lines are fitted polariton dispersions.

4.4 Electrical performance

To evaluate the performance of the polaritonic OLEDs, electrical and optical characterizations were performed. Panels (a–c) of *Figure 30* summarize the behavior of a representative device. The EQE–J characteristics exhibit a peak EQE of 10.64% at low current density, followed by a gradual roll-off with increasing J, reaching $\sim 1\%$ at $10^2\,\mathrm{mA\,cm^{-2}}$; this is consistent with charge-injection imbalance between holes and electrons [60]. The J–V curve shows typical diode behavior with low leakage under reverse bias and a clear turn-on at ~ 3.4 V (**Figure 30b**). The normalized electroluminescence (EL) spectrum is centered at ~ 780 nm, consistent with LP-dominated emission, with a weak shoulder on the short-wavelength side (**Figure 30c**).

Several nominally identical devices were fabricated and measured to assess reproducibility and device-to-device variability. Across the measured device set, the mean peak EQE is $10.54 \pm 1.63\%$ (mean $\pm$ SD), with a maximum of 12.69% at $\lambda_{\mathrm{peak}} \approx 780$ nm. The data shown correspond to the device whose performance is closest to this mean.

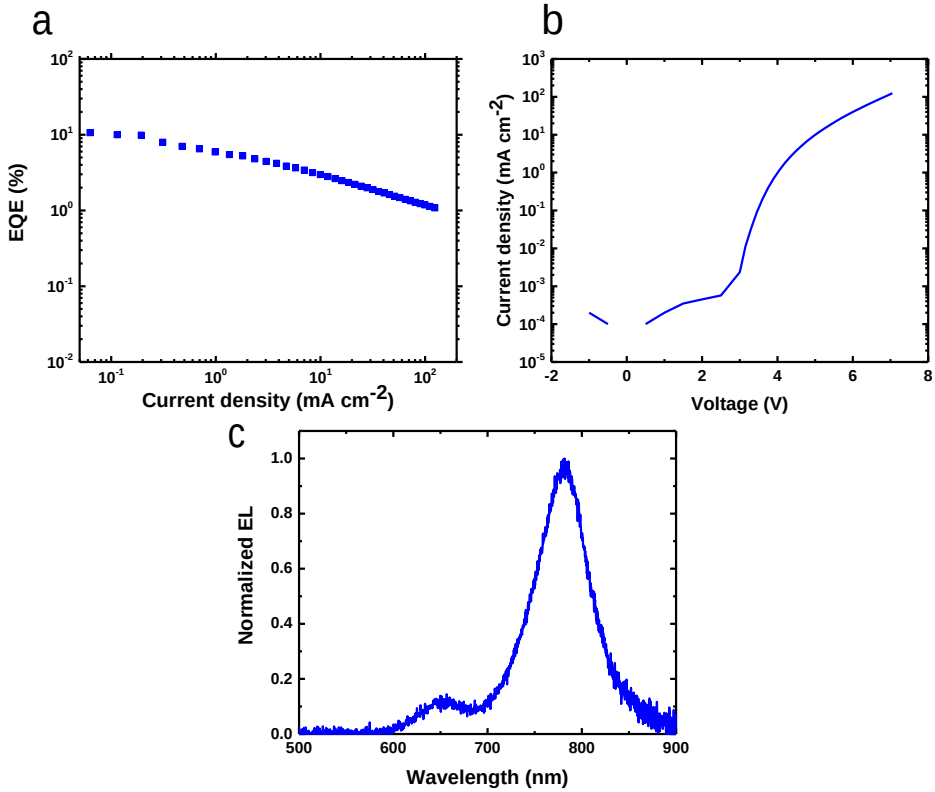

Figure 30. Electrical characterization of a representative polaritonic NIR OLED: (a) EQE–J (b) J–V characteristics (c) normalized EL spectrum

4.5 Angular spectral stability

As discussed in Section 1.2.3, and as demonstrated in the previous chapter for OPDs, the hybrid light–matter character of exciton–photon polaritons can confer remarkable angular stability to the emission; under suitable detuning, the LP acquires predominantly excitonic character. To assess this experimentally, **Figure 31** compares the angle-resolved electroluminescence (AREL) of a polaritonic OLED with that of a reference microcavity OLED (MC-OLED). The MC-OLED was realized by removing the SCL while keeping the remainder of the stack unchanged, and its cavity resonance was adjusted by tuning the TAPC:F6TCNNQ layer thickness so that the emission peak lies close to the LP emission of the polaritonic OLED.

Figure 31 displays false-color AREL maps (intensity vs. wavelength and angle). The polaritonic OLED shows a peak that is only weakly dispersive with angle, consistent with LP-dominated, exciton-like emission, whereas the MC-OLED exhibits a pronounced angle-dependent spectral shift following the cavity dispersion. The inset polar plot summarizes the angular intensity distribution: the polarionic OLED is nearly Lambertian, while the MC-OLED is markedly more directional.

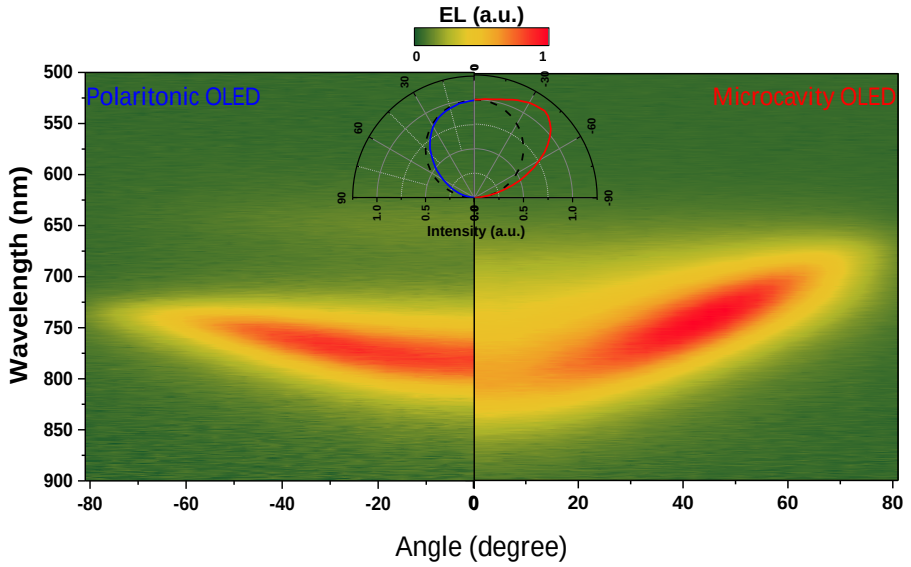

Figure 31. AREL of a polaritonic OLED (left) and a reference microcavity OLED (right). The polaritonic OLED shows weak angular dispersion and near-Lambertian emission, whereas the MC-OLED follows the cavity dispersion and is more directional. Inset: polar intensity profiles.

4.6 Mechanism

Unlike previous reports [11, 61], the NIR polaritonic OLED developed here incorporates two key design features: (i) substantial spectral overlap between the SCL absorption and the EML emission, and (ii) operation in a first-order cavity mode, bringing the EML and SCL into close optical proximity. This motivated an initial investigation of how introducing the SCL into the OLED stack affects the EML emission. To this end, photoluminescence (PL) and EL were measured on a device with the same layer sequence as **Figure 28**, but without the semi-transparent top electrode. The PL and EL spectra are similar and exhibit a distorted lineshape in the spectral region where the SCL absorption overlaps the EML emission (**Figure 32**). This behavior is consistent with energy transfer from the EML to the SCL via radiative re-absorption (EML photons re-absorbed by the SCL) and, to some extent, non-radiative FRET. However, in the present stack, the $\sim$30 nm EML–SCL separation renders direct dipole–dipole FRET negligible; reports of "long-range FRET" generally involve plasmonic, waveguided, or cavity mediation. The SCL shows a strong absorption band peaking at 680 nm with a long-wavelength tail; for $d = 60$ nm this produces wavelength-selective re-absorption of the EML emission predominantly on the short-wavelength side, yielding the observed shoulder/attenuation in the overlap region. As expected, the distortion is strongest around $\sim$650–720 nm and weakens beyond $\sim$760–800 nm, where the SCL absorption diminishes.

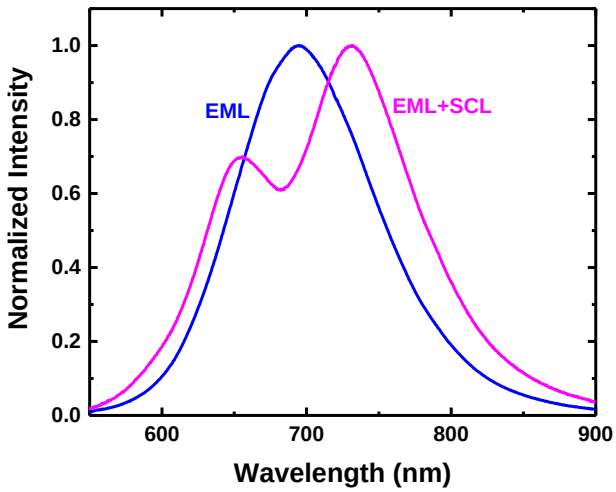

Figure 32. Normalized PL emission spectrum of the device without SCL (EML, 20 wt% DCN-SPTPA in CBP, blue) and device with SCL (Magenta).

Figure 33 shows the angle-resolved electroluminescence (false color) of the polaritonic OLED. The blue curves are coupled-oscillator fits to the MP and LP dispersions. The pink envelope schematically depicts the EML emission after SCL-induced filtering, with blue dashed lines indicating spectral regions where spontaneous emission from the EML radiatively pumps the polariton branches. Based on this picture, it is reasonable to *speculate* that, because the EML spectrum overlaps both MP and LP, radiative pumping injects population into each [6], maintaining finite steady-state occupation of both branches; subsequent scattering/relaxation (downward arrows) then funnels population from MP to LP [62, 63], yielding LP-dominated far-field EL. Direct time-resolved confirmation of MP→LP scattering is not provided here. Moreover, direct MP→LP scattering is expected to be weak due to polariton delocalization (overlap $\propto 1/N$); relaxation may instead proceed via classical pathways such as MP→dark-state reservoir (DS)→LP.

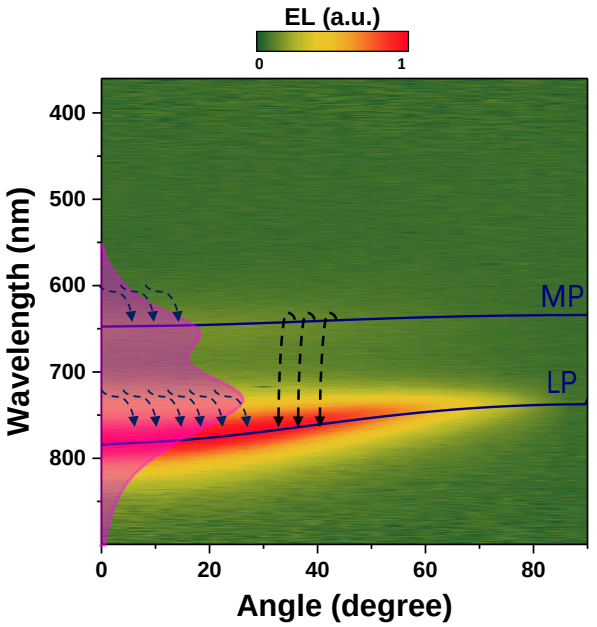

Figure 33. AREL (false color) of Device A. Blue curves are coupled-oscillator fits to the MP and LP dispersions. The pink envelope sketches the EML emission after SCL filtering; arrows from the envelope indicate where radiative pumping from the EML can populate MP and LP. Dashed arrows denote the *speculated* relaxation from MP to LP, consistent with LP-dominated NIR emission near ∼780 nm. Overlaid schematics indicate proposed pumping/relaxation paths and are not quantitative.

4.7 Extended data: Device B

For completeness, additional measurements were carried out on Device B, fabricated with a 70 nm SCL and designed to push the emission peak beyond 800 nm. **Figure 34** summarizes the performance of a representative device. (a) The EQE–J characteristics show a peak efficiency of $\sim 9.75\%$ at low current density. (b) The J–V curve exhibits typical diode behavior with low reverse leakage and a clear turn-on near 3.5 V. (c) The normalized EL spectrum is centered in the NIR at ~ 815 nm, with a weak short-wavelength shoulder (≈ 650 nm) attributable to MP emission; the inset polar plot indicates an above-Lambertian angular profile, consistent with a higher photonic content of the LP. Across the measured device set, Device B exhibits a mean peak EQE of $9.34 \pm 0.92\%$, with maxima up to 10.88%. The data shown correspond to a device whose performance is close to this mean.

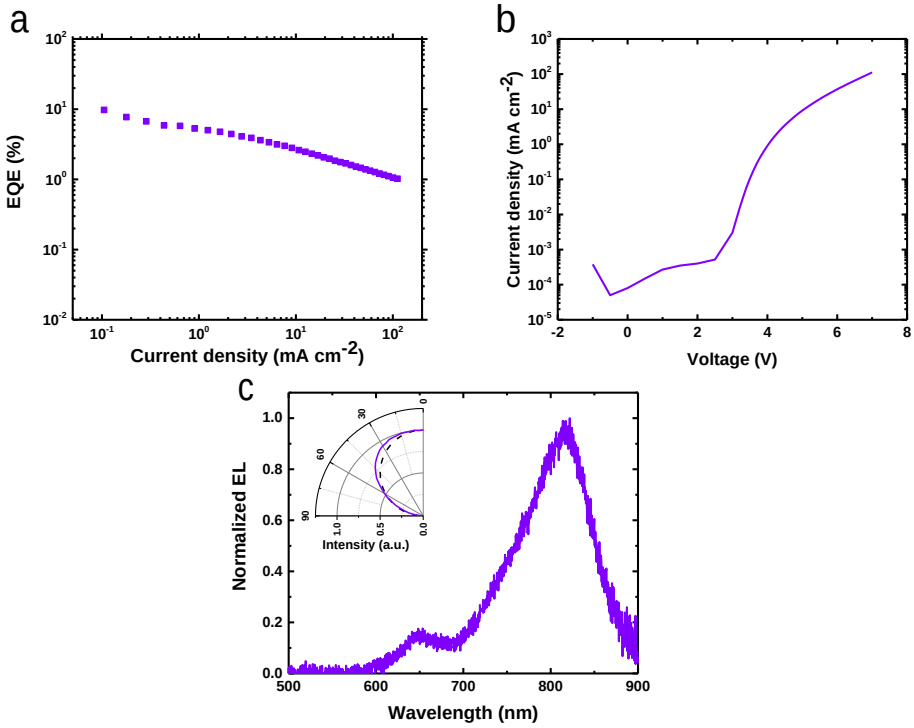

Figure 34. Electrical characterization of a representative polaritonic NIR OLED (device b): (a) EQE–J (b) J–V characteristics (c) normalized EL spectrum. Inset: polar intensity profiles

4.8 State-of-the-art

Figure 35 benchmarks EQE versus peak wavelength for representative purely organic TADF NIR OLEDs from the literature (various symbols; legend at right) alongside this work. Most literature points cluster below $\sim 5\%$ EQE across 750–850 nm, with performance generally declining toward longer wavelengths. In contrast, the devices reported in the thesis achieve markedly higher efficiencies at their respective emission peaks: Device A at $\lambda_{\mathrm{peak}} \approx 780$ nm delivers maximum EQE of 12.69% ($10.54 \pm 1.63\%$), while Device B at $\lambda_{\mathrm{peak}} \approx 815$ nm reaches maximum EQE of 10.88% ($9.34 \pm 0.92\%$). Error bars denote the measured spread within each device set. Together, these results place both devices among the highest-performing purely organic NIR OLEDs near 780 nm and beyond 800 nm [58, 64–76]. Notably, the emission bandwidths are substantially narrower than the field average: the FWHM is 68 nm for Device A and 96 nm for Device B, compared with an average FWHM of ~ 145 nm for representative NIR TADF OLEDs, thereby reducing visible leakage and concentrating emission in the NIR.

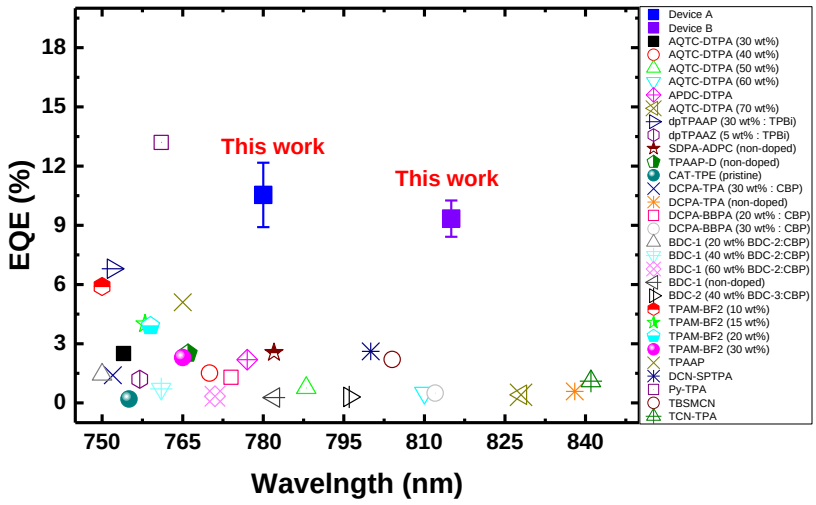

Figure 35. EQE versus peak wavelength for representative NIR OLEDs from the literature (various symbols; legend at right) alongside this work. Blue and purple squares mark Device A ($\lambda_{\mathrm{peak}} \approx 780$ nm) and Device B ($\lambda_{\mathrm{peak}} \approx 815$ nm), respectively; error bars show mean $\pm$ SD. Both devices rank among the highest-performing purely organic NIR OLEDs at their respective wavelengths.

4.9 Conclusions

This chapter demonstrated a polariton-enabled route to efficient NIR emission by combining a broadband deep-red EML (DCN-SPTPA:CBP) with a strong-coupling layer (SubNC) in a first-order microcavity. Angle-resolved reflectivity confirmed strong light–matter coupling, revealing three polariton branches arising from coupling to the SubNC 0–0 and 0–1 excitons. With a 60 nm SCL (Device A), the LP was positioned at $\sim$780 nm, yielding LP-dominated NIR electroluminescence; increasing the SCL to 70 nm (Device B) pushed the emission beyond 800 nm. Angle-resolved EL exhibited weak dispersion and near-Lambertian output for the polaritonic devices as compared to MC-OLEDs. Electrical/optical characterization established competitive efficiencies in the target spectral ranges. Device A achieved a mean peak EQE of $10.54 \pm 1.63\%$ with a maximum of 12.69% at $\lambda_{\text{peak}} \approx 780\ \text{nm}$, while Device B (70 nm SCL) delivered $9.34 \pm 0.92\%$ on average, with maxima up to 10.88% near 815 nm.

Overall, these results show that polaritonic engineering can (i) spectrally concentrate broadband organic emission into the NIR via the LP, (ii) improve angular stability and spectral selectivity, and (iii) sustain high external efficiency at wavelengths where conventional TADF devices typically suffer from enhanced non-radiative loss.

4.10 Author contributions

A.G.A. and K.S.D. initiated the study and, together with A.M. and M.C.G., planned the experiments. **A.G.A.** designed and fabricated the devices, performed the measurements, and analyzed the data. A.M. oversaw the experiments and data analysis. M.C.G. and K.S.D. provided laboratory resources and overall project supervision. All authors discussed the results.

5 Solution-processed microcavities for low-cost polaritonics

This chapter has been adapted from: Palo E, Papachatzakis MA, Abdelmagid AG, Qureshi H, Kumar M, Salomaki M, Daskalakis KS. Developing solution-processed distributed bragg reflectors for microcavity polariton applications. The Journal of Physical Chemistry C. 2023;127(29):14255-62. ***and*** *Qureshi HA, Papachatzakis MA,Abdelmagid AG, Salomäki M, Mäkilä E, Tuomi O, Siltanen O, Daskalakis KS. Giant Rabi Splitting and Polariton Photoluminescence in an all Solution-Deposited Dielectric Microcavity. Advanced Optical Materials. 2025;13(16):2500155*

5.1 Motivation

All device platforms introduced in this thesis to date have employed metal-clad (metal–metal) microcavities. This choice reflects clear practical advantages: metal mirrors are straightforward to evaporate as thin, uniform films at low temperature; compact stacks with small optical mode volumes are readily obtained; and rapid prototyping is possible without complex tooling. At the same time, the semi-transparent top metal is intrinsically lossy. Ohmic and plasmonic absorption lower the cavity quality factor Q, attenuate both in-coupling and out-coupling, and limit the achievable Purcell enhancement. These constraints ultimately cap performance when narrow linewidths and high Q are required.

Dielectric distributed Bragg reflectors (DBRs) offer a contrasting route. Quarter-wave stacks of low-loss dielectrics deliver high reflectivity with negligible absorption in the stopband, enabling much higher Q and eliminating plasmonic loss pathways. Reflectivity and bandwidth are tuned by layer count and index contrast. However, conventional DBR fabrication, physical vapour deposition, atomic layer deposition, or molecular beam epitaxy, is resource- and time-intensive, often involves elevated temperatures or energetic species, and is frequently incompatible with completed organic multilayers. This creates a performance–manufacturability gap: excellent optics in stand-alone cavities but limited integration into device-relevant organic stacks [77, 78].

Solution-processed DBRs aim to bridge this gap. Spin or dip coating, slot-die coating, and inkjet printing allow low-temperature deposition of polymer and sol–gel/oxide layers and nanoparticle composites, reducing cost and simplifying

equipment while remaining compatible with sensitive organic films and flexible substrates. Large-area scalability and straightforward spectral tuning via thickness control follow naturally. The remaining challenges are practical ones: precise thickness and refractive-index control, solvent orthogonality, interlayer adhesion and roughness, and achieving sufficient index contrast without introducing absorption [79–83].

Scope of this chapter: Motivated by these considerations, this chapter introduces low-cost, solution-processed DBR microcavities that retain the optical benefits of dielectric mirrors while remaining compatible with organic device fabrication. The focus is on simple material stacks, gentle processing, and repeatable thickness/index control, establishing a practical pathway for future integration of solution-processed DBRs into polaritonic OPDs and OLEDs.

5.2 Results and discussion

5.2.1 Hybrid metal-DBR microcavity

The first milestone was the demonstration that solution-processed DBRs can be integrated into device-like, hybrid metal–dielectric microcavities and still reach the strong-coupling regime (**Figure 36**). In **Publication IV**, a bottom DBR was fabricated entirely from solution by sequential dip-coating high- and low-index layers (e.g., TiOH/PVA and Nafion), then combined with an aluminum top mirror and an organic spacer (TDAF) to form a planar cavity.
Angle-resolved reflectivity revealed the characteristic UP/LP anticrossing, and polariton photoluminescence was observed at normal incidence, confirming strong coupling in a cavity platform assembled with low-temperature, solution steps. In parallel, we also built an all-dielectric, solution-processed DBR/DBR cavity that achieved a high quality factor with only a few mirror pairs, enabled by an automated dip-coating process yielding uniform sub-100-nm layers. Collectively, these results established solution DBRs as practical, low-loss mirrors compatible with organic stacks, while the hybrid (DBR/Al) device verified that strong coupling and LP emission can be realized in a microcavity architecture relevant to optoelectronic devices.

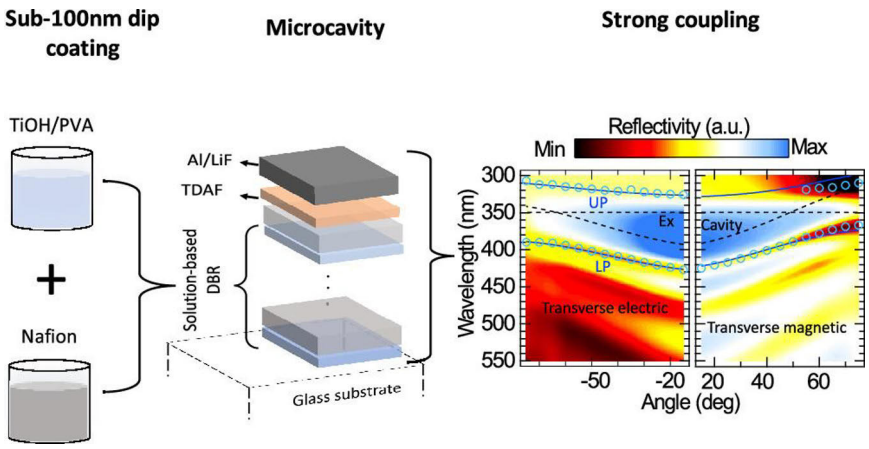

Figure 36. Solution-processed DBR microcavity and strong coupling. Left: sub-100 nm dip-coated dielectric pairs—high-index TiOH/PVA and low-index Nafion—assembled into a bottom distributed Bragg reflector (DBR). Center: planar microcavity stack (glass/solution-DBR/TDAF/Al–LiF). Right: angle-resolved reflectivity for transverse electric (TE) and transverse magnetic (TM) polarizations showing anticrossing between the cavity and exciton (Ex) mode and the emergence of UP and LP.

5.2.2 Fully solution-processed DBR microcavity

Building directly on that platform, **in Publication V**, an all-solution-deposited dielectric microcavity pushed performance further by eliminating the metal contact altogether and retaining full solution compatibility. The structure used Nafion/-TiOH–PVA DBRs (typically with slightly asymmetric pair counts) and a Rhodamine-6G:PVA active layer, with a thin poly-TPD buffer and edge sealing to ensure solvent orthogonality during the second mirror deposition using dip-coating as shown in **Figure 37a and b**.

Angle-resolved reflectivity and photoluminescence confirmed strong coupling with large Rabi splitting, alongside clear LP photoluminescence at normal incidence (**Figure 37c and d**). Notably, the coupling strengths matched or surpassed metal-clad references fabricated by vacuum deposition, while being achieved entirely with spin- and dip-coated layers, an important step toward low-cost, scalable polaritonic optics directly compatible with sensitive organic multilayers.

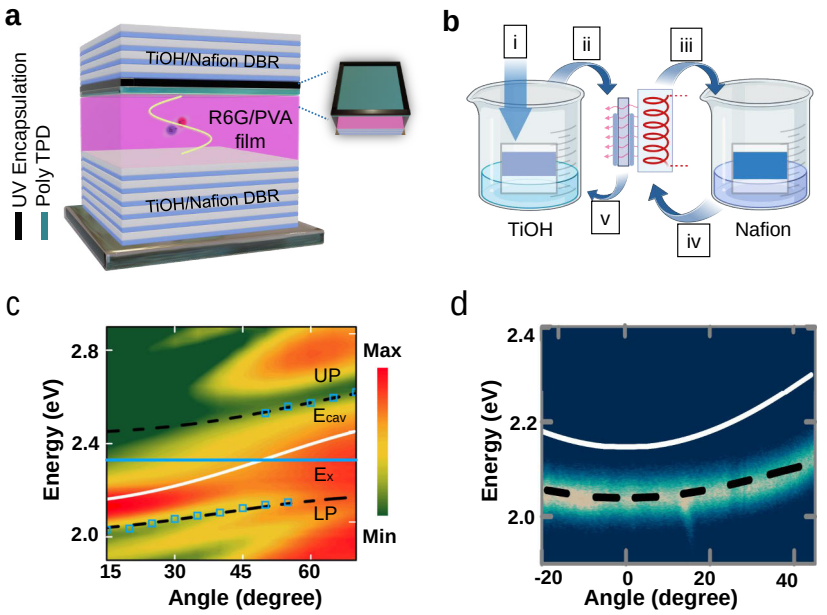

Figure 37. All-solution dielectric microcavity and strong-coupling response. (a) Schematic of a fully solution-processed DBR/DBR cavity: alternating TiOH/PVA (high-index) and Nafion (low-index) mirrors confine an R6G:PVA active film; a thin poly-TPD protection layer and UV encapsulation are used. (b) Dip-coating workflow for DBR fabrication (sequence i–v): sequential deposition of TiOH and Nafion quarter-wave layers with drying/annealing between steps. (c) Angle-resolved reflectivity (false colour) showing anticrossing between the cavity mode (E_{cav}) and exciton resonance (E_x) and the emergence of UP and LP; markers indicate coupled-oscillator fits. (d) Angle-resolved photoluminescence highlighting the LP dispersion (dashed) compared with the bare cavity dispersion (solid).

5.3 Conclusions

Together, these two studies chart a clear trajectory: solution-processed DBRs can deliver high-Q, low-loss mirrors; hybrid DBR/metal cavities validate device-relevant strong coupling and LP emission; and fully dielectric, all-solution microcavities can now reach giant coupling and controlled emission dynamics without resorting to vacuum deposition, laying the groundwork for scalable, device-integrated polaritonics.

5.4 Author contribution

Publication IV: E.P. and M.A.P contributed equally to this work. K.S.D. conceived the project, designed the structures, and guided the experiments. E.P., M.S., and M.P. developed and characterized the solution-processed DBRs. M.P. built the automatized fabrication DBR system. **A.G.A.** and M.K. fabricated the polariton microcavities. H.Q. and **A.G.A.** performed the spectroscopy experiments. E.P., M.P.,

and K.S.D. wrote the manuscript. All authors contributed to the draft and analysis of the data.

Publication V: K.S.D. conceived the project, designed the structures, and guided the experiments. H.A.Q. performed all the fabrications and characterization of the samples. M.P. built the automatized fabrication DBR system. **A.G.A.** fabricated metal-clad microcavities and helped in insulating the DBR samples. O.S. performed the time-resolved photoluminescence analysis. H.A.Q., O.S., and K.S.D. wrote the manuscript. All authors contributed to the draft, discussion, and analysis of the data.

6 Conclusions and future outlook

This thesis set out to bridge the gap between the fundamentals of strong light–matter coupling and the engineering of practical organic optoelectronic devices, identifying where polaritons are *useful* and *competitive* relative to existing technologies.
In **Publication I**, the study examined whether polaritons can modify intramolecular dynamics (e.g., RISC) in working OLEDs. Time-resolved electroluminescence showed that the delayed emission originates from trap states, with no evidence of polariton-induced acceleration of intramolecular processes under electrical injection. A likely reason is the collective, delocalized nature of polaritons: because they spread over N molecules, their overlap with any single-molecule state (e.g., a triplet) scales as $\sim 1/N$, rendering direct coupling negligible in this regime [23, 25]. Under optical pumping, the literature remains divided, underscoring that outcomes are system- and configuration-dependent [17, 18, 23]. **Outlook:** future work should test alternative material platforms, cavity detunings, and excitation schemes that isolate and amplify microscopic channels, under both electrical and optical excitation, to establish a better understanding.

In **Publication II**, the study employed *macroscopic* polaritonic effects to realize narrowband, angle-stable NIR OPDs with competitive responsivity while using unusually thin active layers. By tuning the LP into a region of modest absorption in a PTB7-Th:IEICO-4F blend, the devices combined spectral selectivity with minimal angular dispersion (peak shifts $\sim$ 9–16 nm up to $45°$) and narrow FWHM (< 45 nm), yet maintained state-of-the-art responsivity ($0.23\,\mathrm{A\,W^{-1}}$ at 945/965 nm; $0.11\,\mathrm{A\,W^{-1}}$ at 990 nm at 0 V) with $\sim$ 92–110 nm active layers. This performance compares favorably with cavity-filter OPDs, which require much thicker photoactive films to reach similar responsivity. The key physical lever is the LP excitonic fraction: a higher exciton content flattens the dispersion and suppresses angle dependence, validating a clear structure–property–performance link. **Outlook:** although this chapter focused on macroscopic control, polariton delocalization may also be harnessed to improve transport/collection or noise properties [84]; hybrid strategies that deliberately combine macroscopic cavity design with targeted microscopic pathways present a promising route to even higher detectivity and functionality.

In **Publication III**, the study combined *macroscopic* cavity engineering with *potential* microscopic polaritonic channels (radiative pumping into polariton branches and phonon-assisted MP→LP relaxation) to achieve record NIR performance using a first-order microcavity with a strong-coupling layer. Angle-resolved reflectivity confirmed three polariton branches and sizable Rabi splittings; devices delivered mean peak EQE of $10.54 \pm 1.63\%$ with maxima up to 12.69% at $\sim$ 780 nm (Device A) and $9.34 \pm 0.92\%$ with maxima up to 10.88% at $\sim$ 815 nm (Device B), with bandwidths of 68 nm and 96 nm, respectively, narrower than typical NIR TADF OLEDs. The devices also showed weak angular dispersion and near-Lambertian output, consistent with LP-dominated emission. **Outlook:** priority directions include (i) time-resolved spectroscopy to unambiguously map population pathways (e.g., TRPL, pump–probe), (ii) cavity/outcoupling optimization to further elevate EQE at fixed FWHM, (iii) detuning and materials screening to push emission deeper into the NIR while resisting energy-gap-law losses, and (iv) stability and manufacturability studies toward scalable, flexible form factors.

In **Publication IV and V**, the work establishes a low-cost, solution-processed route to microcavity polaritonics by developing dip-coated DBRs that are compatible with organic device stacks. First, a hybrid solution-DBR/Al cavity with a TDAF spacer exhibited unambiguous strong coupling, angle-resolved reflectivity revealed UP/LP anticrossing and lower-polariton photoluminescence, with Rabi splittings of ~ 750, 803 meV. Second, a fully solution-processed DBR/DBR cavity achieved a quality factor $Q > 91$ with only six mirror pairs and demonstrated "giant" coupling that scales with R6G concentration, together with clear LP emission at normal incidence. These results show that solution DBRs can deliver high-Q, low-loss optics and enable strong coupling without vacuum deposition, charting a practical path toward scalable, device-integrated polaritonics for OPDs and OLEDs.

Overall impact: Collectively, this thesis shows that polaritonics can be deployed *strategically*. While microscopic polaritonic effects may remain difficult to harness in practical devices, macroscopic polaritonic engineering delivers immediate gains in OPDs. Furthermore, by combining microscopic population pathways with macroscopic cavity engineering, polariton-enabled OLEDs achieve record NIR performance while also narrowing the emission spectrum. Thus, the thesis provides concrete, experimentally validated strategies for efficient organic optoelectronics, clarifying where polaritons offer clear, competitive advantages. With continued convergence of materials design, cavity engineering, and time-resolved insights, polaritonic device concepts are poised to become a *transformative* technology for miniaturized, high-performance organic photonics and optoelectronics.

List of References

[1] Anna Köhler and Heinz Bässler. *Electronic processes in organic semiconductors: An introduction*. John Wiley & Sons, 2015.

[2] Alexey Kavokin, Jeremy J Baumberg, Guillaume Malpuech, and Fabrice P Laussy. *Microcavities*. Oxford university press, 2017.

[3] Stephen R Forrest. *Organic electronics: foundations to applications*. Oxford University Press, USA, 2020.

[4] Manuel Hertzog, Mao Wang, Jürgen Mony, and Karl Börjesson. Strong light–matter interactions: a new direction within chemistry. *Chemical Society Reviews*, 48(3):937–961, 2019.

[5] ET Jaynes and FW Cummings. Comparison of quantum and semiclassical radiation theories with a single mode quantized field. *Proc. IEEE*, 51:89–109, 1963.

[6] Juan B Pérez-Sánchez and Joel Yuen-Zhou. Radiative pumping vs vibrational relaxation of molecular polaritons: a bosonic mapping approach. *Nature Communications*, 16(1):3151, 2025.

[7] Gal Sandik, Johannes Feist, Francisco J García-Vidal, and Tal Schwartz. Cavity-enhanced energy transport in molecular systems. *Nature Materials*, 24(3):344–355, 2025.

[8] David M Coles, Niccolo Somaschi, Paolo Michetti, Caspar Clark, Pavlos G Lagoudakis, Pavlos G Savvidis, and David G Lidzey. Polariton-mediated energy transfer between organic dyes in a strongly coupled optical microcavity. *Nature materials*, 13(7):712–719, 2014.

[9] Raj Pandya, Arjun Ashoka, Kyriacos Georgiou, Jooyoung Sung, Rahul Jayaprakash, Scott Renken, Lizhi Gai, Zhen Shen, Akshay Rao, and Andrew J Musser. Tuning the coherent propagation of organic exciton-polaritons through dark state delocalization. *Advanced Science*, 9(18):2105569, 2022.

[10] Xiaolan Zhong, Thibault Chervy, Lei Zhang, Anoop Thomas, Jino George, Cyriaque Genet, James A Hutchison, and Thomas W Ebbesen. Energy transfer between spatially separated entangled molecules. *Angewandte Chemie International Edition*, 56(31):9034–9038, 2017.

[11] Andreas Mischok, Sabina Hillebrandt, Seonil Kwon, and Malte C Gather. Highly efficient polaritonic light-emitting diodes with angle-independent narrowband emission. *Nature Photonics*, 17(5):393–400, 2023.

[12] Julia Witt, Andreas Mischok, Francisco Tenopala Carmona, Sabina Hillebrandt, Julian F Butscher, and Malte C Gather. High-brightness blue polariton organic light-emitting diodes. *ACS photonics*, 11(5):1844–1850, 2024.

[13] Jianbo De, Ruiyang Zhao, Fan Yin, Chunling Gu, Teng Long, Han Huang, Xue Cao, Cunbin An, Bo Liao, Hongbing Fu, et al. Organic polaritonic light-emitting diodes with high luminance and color purity toward laser displays. *Light: Science & Applications*, 13(1):191, 2024.

[14] Elad Eizner, Julien Brodeur, Fábio Barachati, Aravindan Sridharan, and Stéphane Kéna-Cohen. Organic photodiodes with an extended responsivity using ultrastrong light–matter coupling. *ACS Photonics*, 5(7):2921–2927, 2018.

[15] Andreas Mischok, Jan Lüttgens, Felix Berger, Sabina Hillebrandt, Francisco Tenopala-Carmona, Seonil Kwon, Caroline Murawski, Bernhard Siegmund, Jana Zaumseil, and Malte C Gather. Spectroscopic near-infrared photodetectors enabled by strong light–matter coupling in (6, 5) single-walled carbon nanotubes. *The Journal of Chemical Physics*, 153(20), 2020.

[16] Olli Siltanen, Kimmo Luoma, Andrew J Musser, and Konstantinos S Daskalakis. Enhancing the

efficiency of polariton oleds in and beyond the single-excitation subspace. *Advanced Optical Materials*, 13(12):2403046, 2025.

[17] Kati Stranius, Manuel Hertzog, and Karl Börjesson. Selective manipulation of electronically excited states through strong light–matter interactions. *Nature Communications*, 9(1):2273, 2018.

[18] Yi Yu, Suman Mallick, Mao Wang, and Karl Börjesson. Barrier-free reverse-intersystem crossing in organic molecules by strong light-matter coupling. *Nature communications*, 12(1):3255, 2021.

[19] KS Daskalakis, SA Maier, Ray Murray, and Stéphane Kéna-Cohen. Nonlinear interactions in an organic polariton condensate. *Nature materials*, 13(3):271–278, 2014.

[20] Rahul Bhuyan, Jurgen Mony, Oleg Kotov, Gabriel W Castellanos, Jaime Gómez Rivas, Timur O Shegai, and Karl Börjesson. The rise and current status of polaritonic photochemistry and photophysics. *Chemical Reviews*, 123(18):10877–10919, 2023.

[21] Daniele Sanvitto and Stéphane Kéna-Cohen. The road towards polaritonic devices. *Nature materials*, 15(10):1061–1073, 2016.

[22] Francisco J Garcia-Vidal, Cristiano Ciuti, and Thomas W Ebbesen. Manipulating matter by strong coupling to vacuum fields. *Science*, 373(6551):eabd0336, 2021.

[23] Elad Eizner, Luis A Martínez-Martínez, Joel Yuen-Zhou, and Stéphane Kéna-Cohen. Inverting singlet and triplet excited states using strong light-matter coupling. *Science advances*, 5(12):eaax4482, 2019.

[24] Tomohiro Ishii, Juan B Pérez-Sánchez, Joel Yuen-Zhou, Chihaya Adachi, Takuji Hatakeyama, and Stéphane Kéna-Cohen. Modified prompt and delayed kinetics in a strongly coupled organic microcavity containing a multiresonance tadf emitter. *ACS photonics*, 11(10):3998–4007, 2024.

[25] Luis A Martínez-Martínez, Elad Eizner, Stéphane Kéna-Cohen, and Joel Yuen-Zhou. Triplet harvesting in the polaritonic regime: A variational polaron approach. *The Journal of Chemical Physics*, 151(5), 2019.

[26] Stéphane Kéna-Cohen, Stefan A Maier, and Donal DC Bradley. Ultrastrongly coupled exciton–polaritons in metal-clad organic semiconductor microcavities. *Advanced Optical Materials*, 1(11):827–833, 2013.

[27] Christopher R Gubbin, Stefan A Maier, and Stéphane Kéna-Cohen. Low-voltage polariton electroluminescence from an ultrastrongly coupled organic light-emitting diode. *Applied Physics Letters*, 104(23), 2014.

[28] Jai-Pil Choi, Ken-Tsung Wong, You-Ming Chen, Jen-Kan Yu, Pi-Tai Chou, and Allen J Bard. Electrogenerated chemiluminescence. 76. excited singlet state emission vs excimer emission in ter (9, 9-diarylfluorene) s. *The Journal of Physical Chemistry B*, 107(51):14407–14413, 2003.

[29] Jürgen Mony, Yi Yu, Clara Schafer, Suman Mallick, Khushbu Kushwaha, and Karl Börjesson. Interplay between polaritonic and molecular trap states. *The Journal of Physical Chemistry C*, 126(18):7965–7972, 2022.

[30] Ross D Jansen-van Vuuren, Ardalan Armin, Ajay K Pandey, Paul L Burn, and Paul Meredith. Organic photodiodes: the future of full color detection and image sensing. *Advanced Materials*, 28(24):4766–4802, 2016.

[31] Jochen Vanderspikken, Wouter Maes, and Koen Vandewal. Wavelength-selective organic photodetectors. *Advanced Functional Materials*, 31(36):2104060, 2021.

[32] Yazhong Wang, Jonas Kublitski, Shen Xing, Felix Dollinger, Donato Spoltore, Johannes Benduhn, and Karl Leo. Narrowband organic photodetectors–towards miniaturized, spectroscopic sensing. *Materials Horizons*, 9(1):220–251, 2022.

[33] Xingchao Zhao, Jian Wang, Ming Liu, Xiaoling Ma, and Fujun Zhang. Narrowband organic photodetectors: From fundamentals to prospects. *Advanced Optical Materials*, page 2401087, 2024.

[34] Ardalan Armin, Ross D Jansen-van Vuuren, Nikos Kopidakis, Paul L Burn, and Paul Meredith. Narrowband light detection via internal quantum efficiency manipulation of organic photodiodes. *Nature communications*, 6(1):6343, 2015.

[35] Qianqian Lin, Ardalan Armin, Paul L Burn, and Paul Meredith. Filterless narrowband visible photodetectors. *Nature Photonics*, 9(10):687–694, 2015.

[36] Boming Xie, Ruihao Xie, Kai Zhang, Qingwu Yin, Zhicheng Hu, Gang Yu, Fei Huang, and Yong Cao. Self-filtering narrowband high performance organic photodetectors enabled by manipulating localized frenkel exciton dissociation. *Nature communications*, 11(1):2871, 2020.

[37] Quan Liu, Stefan Zeiske, Xueshi Jiang, Derese Desta, Sigurd Mertens, Sam Gielen, Rachith Shanivarasanthe, Hans-Gerd Boyen, Ardalan Armin, and Koen Vandewal. Electron-donating amine-interlayer induced n-type doping of polymer: nonfullerene blends for efficient narrowband near-infrared photo-detection. *Nature Communications*, 13(1):5194, 2022.

[38] John M Lupton, Robert Koeppe, Jürgen G Müller, Jochen Feldmann, Ullrich Scherf, and Uli Lemmer. Organic microcavity photodiodes. *Advanced Materials*, 15(17):1471–1474, 2003.

[39] Bernhard Siegmund, Andreas Mischok, Johannes Benduhn, Olaf Zeika, Sascha Ullbrich, Frederik Nehm, Matthias Böhm, Donato Spoltore, Hartmut Fröb, Christian Körner, et al. Organic narrowband near-infrared photodetectors based on intermolecular charge-transfer absorption. *Nature communications*, 8(1):15421, 2017.

[40] Zheng Tang, Zaifei Ma, Antonio Sánchez-Díaz, Sascha Ullbrich, Yuan Liu, Bernhard Siegmund, Andreas Mischok, Karl Leo, Mariano Campoy-Quiles, Weiwei Li, et al. Polymer: fullerene bimolecular crystals for near-infrared spectroscopic photodetectors. *Advanced Materials*, 29(33):1702184, 2017.

[41] Jing Wang, Sascha Ullbrich, Ji-Ling Hou, Donato Spoltore, Qingwei Wang, Zaifei Ma, Zheng Tang, and Koen Vandewal. Organic cavity photodetectors based on nanometer-thick active layers for tunable monochromatic spectral response. *ACS Photonics*, 6(6):1393–1399, 2019.

[42] Jochen Vanderspikken, Quan Liu, Zhen Liu, Tom Vandermeeren, Tom Cardeynaels, Sam Gielen, Bruno Van Mele, Niko Van den Brande, Benoît Champagne, Koen Vandewal, et al. Tuning electronic and morphological properties for high-performance wavelength-selective organic near-infrared cavity photodetectors. *Advanced Functional Materials*, 32(9):2108146, 2022.

[43] Shen Xing, Vasileios Christos Nikolis, Jonas Kublitski, Erjuan Guo, Xiangkun Jia, Yazhong Wang, Donato Spoltore, Koen Vandewal, Hans Kleemann, Johannes Benduhn, et al. Miniaturized vis-nir spectrometers based on narrowband and tunable transmission cavity organic photodetectors with ultrahigh specific detectivity above 10^{14} jones. *Advanced Materials*, 33(44):2102967, 2021.

[44] Yazhong Wang, Bernhard Siegmund, Zheng Tang, Zaifei Ma, Jonas Kublitski, Shen Xing, Vasileios C Nikolis, Sascha Ullbrich, Yungui Li, Johannes Benduhn, et al. Stacked dual-wavelength near-infrared organic photodetectors. *Advanced Optical Materials*, 9(6):2001784, 2021.

[45] Jinjin Yang, Jun Huang, Ruiming Li, Hui Li, Bin Sun, Qianqian Lin, Ming Wang, Zaifei Ma, Koen Vandewal, and Zheng Tang. Cavity-enhanced near-infrared organic photodetectors based on a conjugated polymer containing [1, 2, 5] selenadiazolo [3, 4-c] pyridine. *Chemistry of Materials*, 33(13):5147–5155, 2021.

[46] JPA Souza, L Benatto, G Candiotto, LS Roman, and M Koehler. Binding energy of triplet excitons in nonfullerene acceptors: the effects of fluorination and chlorination. *The Journal of Physical Chemistry A*, 126(8):1393–1402, 2022.

[47] Xin Song, Nicola Gasparini, Long Ye, Huifeng Yao, Jianhui Hou, Harald Ade, and Derya Baran. Controlling blend morphology for ultrahigh current density in nonfullerene acceptor-based organic solar cells. *ACS Energy Letters*, 3(3):669–676, 2018.

[48] Weitao Yang, Weiming Qiu, Epimitheas Georgitzikis, Eddy Simoen, Jill Serron, Jiwon Lee, Itai Lieberman, David Cheyns, Pawel Malinowski, Jan Genoe, et al. Mitigating dark current for high-performance near-infrared organic photodiodes via charge blocking and defect passivation. *ACS Applied Materials & Interfaces*, 13(14):16766–16774, 2021.

[49] Abu Bakar Siddik, Epimitheas Georgitzikis, Yannick Hermans, Jubin Kang, Joo Hyoung Kim, Vladimir Pejovic, Itai Lieberman, Pawel E Malinowski, Andriy Kadashchuk, Jan Genoe, et al. Interface-engineered organic near-infrared photodetector for imaging applications. *ACS Applied Materials & Interfaces*, 15(25):30534–30542, 2023.

[50] Song Yi Park, Chiara Labanti, Richard A Pacalaj, Tack Ho Lee, Yifan Dong, Yi-Chun Chin, Joel Luke, Gihan Ryu, Daiki Minami, Sungyoung Yun, et al. The state-of-the-art solution-processed single component organic photodetectors achieved by strong quenching of intermolecular emissive state and high quadrupole moment in non-fullerene acceptors. *Advanced Materials*, 35(49):2306655, 2023.

[51] Hoang Mai Luong, Chokchai Kaiyasuan, Ahra Yi, Sangmin Chae, Brian Minki Kim, Patchareepond Panoy, Hyo Jung Kim, Vinich Promarak, Yasuo Miyata, Hidenori Nakayama, et al. Highly sensitive resonance-enhanced organic photodetectors for shortwave infrared sensing. *ACS Energy Letters*, 9(4):1446–1454, 2024.

[52] Xiantao Hu, Zhuoran Qiao, Davide Nodari, Qiao He, Jesika Asatryan, Martina Rimmele, Zhili Chen, Jaime Martín, Nicola Gasparini, and Martin Heeney. Remarkable isomer effect on the performance of fully non-fused non-fullerene acceptors in near-infrared organic photodetectors. *Advanced Optical Materials*, 12(6):2302210, 2024.

[53] Polina Jacoutot, Alberto D Scaccabarozzi, Davide Nodari, Julianna Panidi, Zhuoran Qiao, Andriana Schiza, Alkmini D Nega, Antonia Dimitrakopoulou-Strauss, Vasilis G Gregoriou, Martin Heeney, et al. Enhanced sub-1 ev detection in organic photodetectors through tuning polymer energetics and microstructure. *Science Advances*, 9(23):eadh2694, 2023.

[54] Andrea Zampetti, Alessandro Minotto, and Franco Cacialli. Near-infrared (nir) organic light-emitting diodes (oleds): challenges and opportunities. *Advanced Functional Materials*, 29(21):1807623, 2019.

[55] Paloma L dos Santos, Patrycja Stachelek, Youhei Takeda, and Piotr Pander. Recent advances in highly-efficient near infrared oled emitters. *Materials Chemistry Frontiers*, 8(7):1731–1766, 2024.

[56] Shabnam Ahadzadeh, Sonny Brebels, Wouter Maes, and Wim Deferme. Strategies for advancing near-infrared organic light-emitting diodes: Innovations in luminescent materials, device architectures, fabrication methods, and applications. *Advanced Functional Materials*, page 2419599, 2025.

[57] Yuxin Xiao, Hailan Wang, Zongliang Xie, Mingyao Shen, Rongjuan Huang, Yuchen Miao, Guanyu Liu, Tao Yu, and Wei Huang. Nir tadf emitters and oleds: challenges, progress, and perspectives. *Chemical Science*, 13(31):8906–8923, 2022.

[58] Hui Wang, Kai Wang, Jia-Xiong Chen, Xi Zhang, Lu Zhou, Xiao-Chun Fan, Ying-Chun Cheng, Xiao-Yao Hao, Jia Yu, and Xiao-Hong Zhang. Enabling record-high deep-red/near-infrared electroluminescence through subtly managing intermolecular interactions of a thermally activated delayed fluorescence emitter. *Advanced Functional Materials*, 33(41):2304398, 2023.

[59] Andreas Mischok, Bernhard Siegmund, Florian Le Roux, Sabina Hillebrandt, Koen Vandewal, and Malte C Gather. Breaking the angular dispersion limit in thin film optics by ultra-strong light-matter coupling. *Nature Communications*, 15(1):10529, 2024.

[60] Thi Na Le, Hye Yeon Park, Ji Eun Lee, Yerin Kim, Yun-Hi Kim, and Min Chul Suh. Efficiency roll-off suppression in solution-processed organic light-emitting diodes through a bipolar host design. *ACS Materials Letters*, 6(4):1256–1263, 2024.

[61] Jui-Fen Chang, Tong-Yu Lin, Chia-Fu Hsu, Szu-Yu Chen, Shun-Yu Hong, Guo-Sian Ciou, Cheng-Chung Jaing, and Cheng-Chung Lee. Development of a highly efficient, strongly coupled organic light-emitting diode based on intracavity pumping architecture. *Optics Express*, 28(26):39781–39789, 2020.

[62] Tersilla Virgili, D Coles, AM Adawi, C Clark, P Michetti, SK Rajendran, Daniele Brida, Dario Polli, G Cerullo, and DG Lidzey. Ultrafast polariton relaxation dynamics in an organic semiconductor microcavity. *Physical Review B—Condensed Matter and Materials Physics*, 83(24):245309, 2011.

[63] N Somaschi, L Mouchliadis, D Coles, IE Perakis, DG Lidzey, PG Lagoudakis, and PG Savvidis. Ultrafast polariton population build-up mediated by molecular phonons in organic microcavities. *Applied Physics Letters*, 99(14), 2011.

[64] Yi Yuan, Yun Hu, Ye-Xin Zhang, Jiu-Dong Lin, Ya-Kun Wang, Zuo-Quan Jiang, Liang-Sheng Liao, and Shuit-Tong Lee. Over 10% eqe near-infrared electroluminescence based on a thermally activated delayed fluorescence emitter. *Advanced Functional Materials*, 27(26):1700986, 2017.

[65] Jin-Feng Cheng, Ze-Hui Pan, Kai Zhang, Yue Zhao, Chuan-Kui Wang, Lei Ding, Man-Keung Fung, and Jian Fan. Interrupted intramolecular donor-acceptor interaction compensated by strong through-space electronic coupling for highly efficient near-infrared tadf with emission over 800 nm. *Chemical Engineering Journal*, 430:132744, 2022.

[66] Jie Xue, Jingyi Xu, Jiajun Ren, Qingxin Liang, Qi Ou, Rui Wang, Zhigang Shuai, and Juan Qiao. Intermolecular charge-transfer aggregates enable high-efficiency near-infrared emissions by nonadiabatic coupling suppression. *Science China Chemistry*, 64(10):1786–1795, 2021.

[67] Jing-Feng Liu, Xue-Qi Wang, You-Jun Yu, Sheng-Nan Zou, Sheng-Yi Yang, Zuo-Quan Jiang, and Liang-Sheng Liao. Highly efficient near-infrared thermally activated delayed fluorescence material based on a spirobifluorene decorated donor. *Organic Electronics*, 91:106088, 2021.

[68] Jin-Feng Cheng, Fan-Cheng Kong, Kai Zhang, Jia-Heng Cai, Yue Zhao, Chuan-Kui Wang, Jian Fan, and Liang-Sheng Liao. Positive isotope effect in thermally activated delayed fluorescence emitters based on deuterium-substituted donor units. *Chemical Engineering Journal*, 430:132822, 2022.

[69] Daniel G Congrave, Bluebell H Drummond, Qinying Gu, Stephanie Montanaro, Haydn Francis, Víctor Riesgo-González, Weixuan Zeng, Campbell SB Matthews, Simon Dowland, Iain A Wright, et al. A solution-processable near-infrared thermally activated delayed fluorescent dye with a fused aromatic acceptor and aggregation induced emission behavior. *Journal of Materials Chemistry C*, 10(12):4831–4836, 2022.

[70] You-Jun Yu, Yun Hu, Sheng-Yi Yang, Wei Luo, Yi Yuan, Chen-Chen Peng, Jin-Feng Liu, Aziz Khan, Zuo-Quan Jiang, and Liang-Sheng Liao. Near-infrared electroluminescence beyond 800 nm with high efficiency and radiance from anthracene cored emitters. *Angewandte Chemie International Edition*, 59(48):21578–21584, 2020.

[71] Dae-Hyeon Kim, Anthony D'aléo, Xian-Kai Chen, Atula DS Sandanayaka, Dandan Yao, Li Zhao, Takeshi Komino, Elena Zaborova, Gabriel Canard, Youichi Tsuchiya, et al. High-efficiency electroluminescence and amplified spontaneous emission from a thermally activated delayed fluorescent near-infrared emitter. *Nature Photonics*, 12(2):98–104, 2018.

[72] Afshin Shahalizad, Alexandre Malinge, Lei Hu, Grégory Laflamme, Louis Haeberlé, David M Myers, Jian Mao, William G Skene, and Stéphane Kéna-Cohen. Efficient solution-processed hyperfluorescent oleds with spectrally narrow emission at 840 nm. *Advanced Functional Materials*, 31(1):2007119, 2021.

[73] Jie Xue, Qingxin Liang, Rui Wang, Jiayue Hou, Wenqiang Li, Qian Peng, Zhigang Shuai, and Juan Qiao. Highly efficient thermally activated delayed fluorescence via j-aggregates with strong intermolecular charge transfer. *Advanced Materials*, 31(28):1808242, 2019.

[74] Jing-Wen Tai, Yukun Tang, Kai Zhang, Chen-Zong Yang, Ze-Hui Pan, Yu-Ching Lin, Yu-Wei Shih, Chia-Hsun Chen, Tien-Lung Chiu, Jiun-Haw Lee, et al. 13.2% eqe near-infrared tadf oled with emission peak at 761 nm. *Chemical Engineering Journal*, 452:139534, 2023.

[75] Ying Yu, Hao Xing, Dan Liu, Mengying Zhao, Herman H-Y Sung, Ian D Williams, Jacky WY Lam, Guohua Xie, Zheng Zhao, and Ben Zhong Tang. Solution-processed aiegen nir oleds with eqe approaching 15%. *Angewandte Chemie*, 134(26):e202204279, 2022.

[76] Jing-Xing Liang, Yukun Tang, Xiaofei Wang, Kai Zhang, Yu-wei Shih, Chia-Hsun Chen, Tien-Lung Chiu, Pei Jin Li, Jiun-Haw Lee, Chuan-Kui Wang, et al. Highly efficient near-infrared thermally activated delayed fluorescence organic light-emitting diodes with emission beyond 800 nm. *Journal of Materials Chemistry C*, 11(21):6981–6988, 2023.

[77] Russell Holmes and Stephen Forrest. Strong exciton-photon coupling in organic materials. *Organic Electronics*, 8:77–93, 2007.

[78] K. E. McGhee, A. Putintsev, R. Jayaprakash, K. Georgiou, M. E. O'Kane, R. C. Kilbride, E. J. Cassella, M. Cavazzini, D. A. Sannikov, and P. G. Lagoudakis. Polariton condensation in an organic microcavity utilising a hybrid metal-DBR mirror. *Scientific Reports*, 11:20879, 2021.

[79] Paola Lova, Gianluca Manfredi, and Davide Comoretto. Advances in functional solution processed planar 1d photonic crystals. *Advanced Optical Materials*, 6:1800730, 2018.

[80] Sebastian Guldin. *Inorganic Nanoarchitectures by Organic Self-Assembly*. Springer, 2013.

[81] S. Bachevillier, H. K. Yuan, A. Strang, A. Levitsky, G. L. Frey, A. Hafner, D. D. Bradley, P. N. Stavrinou, and N. Stingelin. Fully solution-processed photonic structures from inorganic/organic molecular hybrid materials and commodity polymers. *Advanced Functional Materials*, 29:1808152, 2019.

[82] C. Bronnbauer, A. Riecke, M. Adler, J. Hornich, G. Schunk, C. J. Brabec, and K. Forberich. Printing of large-scale, flexible, long-term stable dielectric mirrors with suppressed side interferences. *Advanced Optical Materials*, 6:1700518, 2018.

[83] Q. Zhang, Q. Jin, A. Mertens, C. Rainer, R. Huber, J. Fessler, G. Hernandez-Sosa, and U. Lemmer. Fabrication of bragg mirrors by multilayer inkjet printing. *Advanced Materials*, 34:2201348, 2022.

[84] Mao Wang, Manuel Hertzog, and Karl Börjesson. Polariton-assisted excitation energy channeling in organic heterojunctions. *Nature communications*, 12(1):1874, 2021.

TURUN
YLIOPISTO
UNIVERSITY
OF TURKU

Painosalama, Turku, Finland 2025

ISBN 978-952-02-0397-9 (PRINT)
ISBN 978-952-02-0398-6 (PDF)
ISSN 2736-9390 (Painettu/Print)
ISSN 2736-9684 (Sähköinen/Online)